TÉCNICO LISBOA

Design of a passive photonic integrated circuit for QKD

Pedro Ricardo Neto Mendes

Thesis to obtain the Master of Science Degree in

Engineering Physics

Supervisors: Prof. Manfred Niehus
Prof. João Carlos Carvalho de Sá Seixas

Examination Committee

Chairperson: Prof. Pedro Miguel Félix Brogueira
Supervisor: Prof. João Carlos Carvalho de Sá Seixas
Member of the Committee: Prof. Paulo Sérgio De Brito André

December 2020

Acknowledgments

What is entanglement?

"Algebra muito simples gone bananas."

Beatriz Dias

Although the structure was taken out of a template found on the internet, the words are sincere.

Throughout the writing of this thesis I have received a great deal of support and assistance.

I would first like to thank my supervisor, Professor Manfred Niehus, whose expertise allowed me to learn a lot during this year. Even though we spent little time in the lab, I was taught so many things that I only hope I can remember them all in the future.

I would like to acknowledge my colleagues from the QuTe Lab for their companionship. I would also like to thank the Physics of Information and Quantum Technology group for their warm welcome. Especially Professor Yasser Omar.

In addition, I have to express my gratitude to my parents for their help in my journey. I was always given the support and space I needed to follow my path.

Finally, I could not have completed this dissertation without my friends. I cannot name every person that helped me get here. From my university friends who had to endure me almost everyday to the friends I could only be with a few times during this time, you have all given me the strength, knowledge and motivation to finish this. And well, my live would be pretty boring (awful really) without you.

Resumo

A informação é um dos recursos mais fundamentais do nosso mundo. Para a manter segura, a distribuição de chaves quânticas está a ser desenvolvida e implementada em todo o mundo. Em Portugal, foi feita uma prova de implementação de princípios. Agora, para a levar para o nível seguinte, é necessário torná-la mais resiliente, robusta e eficiente. Esta tese aborda este objectivo com a intenção de conceber um novo sistema que melhore o actual e que seja possível de melhorar no futuro. Para tal, a fabricação a laser de femtosegundo é analisada como um método de fabricação de um circuito integrado fotónico passivo capaz de realizar QKD. Este processo mostra um grande potencial para produzir um dispositivo deste tipo. O dispositivo é concebido passo a passo, desde guias de onda a acopladores direccionais. É proposto um esquema para o circuito fotónico. Embora não fabricado e testado, em comparação com outros trabalhos, funcionaria, embora algumas interacções fossem necessárias para atingir a sua máxima eficiência. Além disso, foi explorada uma nova fonte de fotões. Uma caracterização experimental completa está a ser feita com base no estudo teórico e nas simulações aqui apresentadas.

Palavras-chave: Informação Quântica, Fotónica, Óptica Integrada, Óptica de Guia de Ondas, Óptica Não Linear.

Abstract

Information is one of the most fundamental resources in our world. To keep it safe, quantum key distribution is being developed and implemented all over the world. In Portugal, a proof-of-principle implementation has been done. Now, to take it to the next level, it must be made more resilient, robust and efficient. This thesis approaches this aim intending to design a new system that improves on the current one and will be possible to refine in the future. To do this, femtosecond laser fabrication is analysed as a fabrication method for a passive photonic integrated circuit capable of performing QKD. This process shows great potential to produce such a device. The device is designed step by step from waveguides to directional couplers. A blueprint for the photonic circuit is proposed. While not fabricated and tested, by comparison to other works, it would work, although some interactions would be necessary to reach its maximum efficiency. In addition, a new photon source was explored. A full experimental characterization is being made based on the theoretical study and simulations presented here.

Keywords: Quantum Information, Photonics, Integrated Optics, Waveguide Optics, Nonlinear Optics.

Contents

Acknowledgments . . . iii

Resumo . . . v

Abstract . . . vii

List of Tables . . . xi

List of Figures . . . xiii

List of Abbreviations . . . xvii

1 Introduction **1**

1.1 Motivation and objectives . . . 1

1.2 State of the art . . . 2

1.3 Thesis Overview . . . 4

2 Quantum Key Distribution - From protocols to systems **5**

2.1 The quantum mechanics of quantum communication . . . 5

2.2 QKD examples . . . 8

2.3 Implementation aspects . . . 12

2.4 Spatial mode mixing with bulk optical components . . . 13

2.5 Secure networking on intercontinental scales - the need for satellite based QKD . . . 15

3 Analysis of femtosecond laser fabrication for integrated photonic waveguides **17**

3.1 Background . . . 17

3.2 Modification regimes induced by laser intensity . . . 18

3.3 Modification regimes induced by the laser's repetition rate . . . 23

3.4 Different writing configurations for waveguide inscription in glasses . . . 24

4 Analysis and design of integrated waveguide based spatial mode mixing with polarization control for QKD **25**

4.1 Background . . . 25

4.2 Development of integrated optical components . . . 27

4.3 Integrated photonic design for QKD . . . 40

4.4 Chapter overview and discussion . . . 43

5 Towards an efficient photon pairs source **45**

5.1 Analysis of spontaneous parametric down-conversion 46

5.2 Applications 58

5.3 Progress and future work 58

6 Conclusion and outlook **61**

Bibliography **63**

List of Tables

2.1 Definition of the information stored in the polarization of a photon. $|D\rangle$ correspond to the diagonal polarization, $|A\rangle$ to the anti-diagonal polarization, $|R\rangle$ to the right circular polarization and $|L\rangle$ to the left circular polarization. 7
2.2 Possible outcomes of the BB84 protocol. In the end, only half the bits are kept and used to create the sifted key. 9
2.3 Example of possible bit error induced by the presence of Eve. 9

4.1 6 common examples of normalized Jones vectors. 26
4.2 Propagation loss of some FLDW waveguides and the laser parameters used. 42

List of Figures

2.1 Bloch sphere representation of a qubit. [41] 6

2.2 Drawing of a Poincaré sphere, which illustrates the space of possible polarizations of electromagnetic waves. [42] 6

2.3 Schematic of a general QKD setup 12

2.4 Schematic of the emitter (Alice) used for the BB84 14

2.5 Optical setup of the emitter (Alice) used for the BB84 protocol. 15

3.1 Schematic representation of nonlinear photoionisation processes underlying femtosecond laser machining. (a) No photoionisation, (b) Tunnelling Ionisation (c) Multi-photon Ionisation 18

3.2 Schematic illustration of key steps in femtosecond-laser-induced structural change in bulk transparent materials [55] 19

3.3 (a): SEM image of a written line in the xz plane, E: electric field of the writing laser, k: wave vector of the writing laser beam (λ = 800 nm, τ_p =150 fs, Ep = 0.5 μJ, V = 100 μm/s, Rep = 250 kHz). (b): The region between two dotted lines is used for calculation. Corresponding normalized correlation functions calculated along the x (c) and z (d) axis. [67] 20

3.4 Schematic arrangement for the stressed waveguide fabrication where $\vec{E}_V$ and $\vec{E}_H$ indicate the electric field orientation for Vertical, V, and Horizontal, H, waveguide polarization eigenmodes, while $\vec{E}_{Par\parallel}$ and $\vec{E}_{Per\perp}$ represent the parallel and perpendicular polarizations of the writing laser, respectively. The insets show microscope end view images of the Bragg grating waveguides sandwiched with vertical (left) and horizontal (right) stress tracks. [68] 21

3.5 Conceptual scheme of the method enabling the direct writing of optical waveguides acting as integrated waveplates with tilted axis. (a) Traditional writing scheme adopting a focusing objective with moderate NA; the symmetry of the writing layout creates birefringent waveguides with the optical axis (OA) aligned as the writing beam direction; actual waveguide writing is performed by a transverse translation of the glass sample (indicated by the purple arrow). (b) Equivalent waveguides can be created by underfilling a high-NA oil-immersion objective. (c) Offsetting the writing beam before the objective results in waveguide writing with an inclined laser beam; the resulting waveguide has an optical axis tilted by an angle y that depends on the amount of offset d of the writing beam with respect to the objective axis. (d) Reduced beam size and offset at the objective aperture is achieved by a small transverse shift of a long focal lens placed at a distance L from the focusing objective.[72] 22
3.6 Schematic of the thermal regimes [78] 23
3.7 Schematic of inscription processes [78]. 24

4.1 Left side: Common types of waveguides [86]. Right side: Schematic representation of a slab waveguide. 27
4.2 Schematic representation of the TE guided modes for a certain height of the slab. [87] . . 29
4.3 Left side: Example of a waveguide fabricated by femtosecond laser machining [89]. Right side: Dispersion curves for low order Linearly Polarized (LP) Modes of an Optical Fiber [90]. 29
4.4 Diagram illustrating the velocity approach to the determination of radiation loss. [95] . . 33
4.5 (a) Microscope images of s-bends (R=3 mm) with input and output waveguide separations of 125, 250, 375 and 500 μm from top to bottom respectively. (b) Bend loss in function of bend radius for different waveguide separations. [54] 34
4.6 Schematic diagram of an S-shaped waveguide bend with a transition length l and a lateral offset h. 34
4.7 Design of a directional coupler with the control parameters represented. 36
4.8 Experimental measurements of the transmission T of DCs with different interaction length L and waveguide separation d=12.5 μm, for H (red circles) and V (blue triangles) polarised input light. Solid lines are best-fitting theoretical curves. Error bars are smaller or comparable to the marker size.[73] 39
4.9 Example of how the polarizing beam coupler can be used to replace the polarizing beam splitter. 40
4.10 Schematic design of a possible integrated photonic circuit to reproduce the BB84 protocol. 41
4.11 Same design as in figure 4.10 with the correct size and scale. 42
4.12 3D schematic implementation of the design studied. The different images show the output polarization (a red line) as a function of which input is on. Upper Left: Horizontal polarization. Upper Right: Vertical polarization. Lower Left: Diagonal polarization. Lower Right: Anti-Diagonal polarization. 43

5.1 The phase matching conditions. Left: The energy of the pump is equal to the sum of the energy of the signal and idler. Center: When angle phase matched, the pump and down converted modes are usually non-collinear. The wave vectors obey momentum conservation. Right: When pumped in a collinear geometry momentum is still conserved. [103] 45
5.2 Sinc function (unnormalized). [105] 50
5.3 Addition of amplitude contributions from different parts of the crystal. Only with phase matching, a high conversion efficiency can be achieved. [106] 50
5.4 A representation of the pump wave vector inside the crystal: the optic axis, OA, lies in the x-z plane making an angle ψ with the z axis. In general, $\vec{k_p}$ does not lie in the x-z plane, but makes an angle θ_p with OA, and an angle ϕ_p with the z axis. $\vec{k_\perp}$ is the projection of $\vec{k_p}$ into the x-y plane, making an angle ϕ_p with the x axis. [107] 51
5.5 Effective nonlinear coefficient in a periodic material. The nonlinear coefficient can be written as a step function, which goes from $-\chi_0^{(2)}$ to $\chi_0^{(2)}$, with a period of Λ. [109] 52
5.6 Theoretical phase matching curves for PPKTP samples. On the left, a period of $\Lambda = 10\,\mu m$. On the right $\Lambda = 10.35\,\mu m$. 54
5.7 Normalized simulated spectral densities for two different values of $|\mathbf{q_s}|$ and a fixed value of temperature. On the left $|\mathbf{q_s}| = 0\,\mu m^{-1}$, on the right $|\mathbf{q_s}| = 0.5\,\mu m^{-1}$ 55
5.8 Sketch of colored emission rings. [110] 56
5.9 Normalized simulated spectral densities for two different temperatures (30°C and 60°C respectively) and a fixed value of transverse momentum ($|\mathbf{q_s}| = 0$). 56
5.10 Normalized simulated spectral densities for two different values of $|\mathbf{q_s}|$ and a fixed value of temperature. On the left $|\mathbf{q_s}| = 0\,\mu m^{-1}$, on the right $|\mathbf{q_s}| = 0.2\,\mu m^{-1}$ 57
5.11 Normalized simulated spectral densities for two different temperatures (30°C and 60°C respectively) and a fixed value of transverse momentum ($|\mathbf{q_s}| = 0\,\mu m^{-1}$). 57
5.12 Characterization of one of the band-pass filters used. 59
5.13 Image from the quTau software while it is connected to signal generators to simulate incoming photons. 60

List of Abbreviations

BER	Bit error rate
CMOS	Complementary metal–oxide–semiconductor
CV	Continuous Variables
DV	Discrete Variables
DOF	Degrees Of Freedom
FLDW	Femtosecond Laser Direct Write
LEO	Low Earth Orbit
LDW	Laser Direct Writing
LP	Linearly Polarized
MM	Multi-Mode
MPI	Multiphoton Ionisation
NA	Numerical Aperture
OAM	Orbital Angular Momentum
PIC	Photonic Integrated Circuit
PPKTP	Periodically Poled Potassium Titanyl Phosphate
QKD	Quantum Key Distribution
RSA	Rivest-Shamir-Adleman
SatQKD	Satellite Quantum Key Distribution
SEM	Scanning Electron Microscope
SM	Single Mode
SPDC	Spontaneous parametric down-conversion
TE	Transverse electric
TEM	Transverse electromagnetic
TM	Transverse magnetic
ULW	Ultraviolet laser writing
VCSEL	Vertical-cavity surface-emitting laser

Chapter 1

Introduction

1.1 Motivation and objectives

It is believed that we are now amid the second quantum revolution [1, 2]. The discovery and development of quantum mechanics marked the first quantum revolution [3, 4]. We used quantum mechanics to understand what already existed. We could explain how metals and semiconductors behaved, but not control or manipulate that behavior. Inventions such as the laser and the transistor, the basic building block of computers, were built following these rules. This approach has given us many of the core technologies underpinning modern society.

The second quantum revolution aims at applying quantum mechanics in every aspect of our lives. The difference between science and technology is the ability to engineer your surroundings to your own ends, and not just explain them. We go from passive observers of the quantum world to actively employing quantum mechanics to alter the world. For example, besides explaining the periodic table, we can make new artificial atoms - quantum dots and excitons - which we can engineer to have electronic and optical properties of our own choosing.

Thus, although quantum mechanics as a science has matured substantially, quantum engineering as a technology is now emerging on its own right. We can attribute this development to practical reasons: as we reach smaller and smaller scales, we need to manipulate the quantum effects to continue improvement; and to more fundamental reasons: the principles of quantum mechanics appear to offer access to a range of new resources.

We can divide quantum technology into three main sub-fields, quantum computing, quantum metrology and quantum communication. Quantum computation has become very popular since the development of Shor's algorithm [5], a quantum algorithm for factoring integers that has the potential to decrypt RSA-encrypted communications (the global standard). This results from the algorithm use of quantum proprieties, which makes it almost exponentially faster than the most efficient known classical factoring algorithm. Quantum computers may have the potential to surpass classical computers in some tasks, and because of that many groups worldwide seek to bring these theoretical results into reality. Many physical realizations of such a computer are being developed using different approaches: small superconducting

circuits [6], the internal state of trapped ions [7], the electronic or nuclear spin of nitrogen-vacancy centers in diamond [8, 9] and many more.

One of the fundamental building blocks of science is the act of measurement. As there are fundamental limits on uncertainty, there are limits to how precise a measurement can be. Remarkably, the exploitation of quantum systems to estimate unknown parameters overcomes the precision limits that can be in principle be reached by using only classical resources [10]. Quantum metrology aims at reaching the ultimate fundamental bounds on estimation precision by exploiting quantum probes and it can benefit different research branches such as measurement on biological systems [11, 12], gravitational waves detection [13], atomic clocks [14], among others.

Information is an essential resource to everyone and to the current society. Communication is then a key aspect of our lives, as it is the way we exchange information between two parties. In order to guarantee the security of any communication, we can use QKD. Quantum Key Distribution protocols have attracted a lot of attention since the first proposal in 1984 [15]. QKD is a secure communication method which implements a cryptographic protocol making use of the principles of quantum physics. It enables two parties to produce a shared random secret key known only to them, which can then encrypt and decrypt messages.

This revolution is of great importance to the entire world, and therefore there are efforts from many countries and groups to lead and have a powerful presence. In Europe, the Quantum Technologies Flagship launched in October 2018 has an expected budget of 1 billion euros over ten years to support the work of quantum researchers [16].

There are many ways of working with quantum systems. The one explored in this work is with photons. A photon's multiple degrees of freedom can be prepared in distinct states and manipulated using conventional optical components such as waveplates and beamsplitters. Photons do not easily interact with one another or with the environment, meaning that noise because of a quantum state interacting with its surroundings is virtually eliminated. Using these conventional components, the size of the devices becomes too big for small-scale applications. To overcome this problem, quantum circuits, similar to electronic circuits, can be developed. The ability to have high density complex designs has encouraged the on-chip integration of photonic quantum circuits.

This thesis work is part of a bigger project with the goal of realizing satellite-to-ground quantum key distribution. In order to do this, I set to develop an approach that would allow us to miniaturize and improve the current quantum key distribution setup while also studying how to make it able to perform satellite-to-ground quantum key distribution.

1.2 State of the art

At present, QKD systems are commercially available. These systems currently rely mostly on attenuated laser pulses rather than single photons. This means a laser beam, a stream of photons, is attenuated until, on average, we have a train of single photons. However, this differs from true single photon sources as the photon distribution follows a Poisson distribution, meaning sometimes there will be over one photon

and other times they will be none.

Before QKD can be widely adopted, it faces several important challenges such as secret key rate, distance, size, cost and practical security [17]. If the secret key rate is small, the number of photons we can send is low, we will not have a secret key the size needed to encrypt messages. The range of communication is limited to field of view or to optical fibers. Optical fibers limit the distance a photon can travel without interference to around 100 km and restrict it to point-to-point communication.

Recently, Satellite Quantum Key Distribution (SatQKD) has proved able to overcome the range limits, enabling secure communication globally. The Chinese mission, known as Micius [18], successfully demonstrated various quantum communication protocols in space [19–21]. These groundbreaking results have spurred an international space race aiming not only to establish the first global quantum communication network but also to develop and deploy the architecture to merge different quantum technologies, such as sensing and computing, to build the future quantum internet. Besides China, other countries and space agencies are designing SatQKD missions involving one or more satellites, including Japan [22], Canada [23], Austria/France (NanoBob) [24] and more. The projects mentioned above address mostly Low Earth Orbit (LEO) satellites, but there is a growing interest for higher orbits as well [25]. Satellites smaller and cheaper than Micius, such as nano-satellites (with a mass ≈10 kg) have been in the spotlight [26], for the possibility of establishing quantum communication services using a constellation [27].

Most of the impressive proof-of-principle demonstrations of photonic quantum technologies found in the literature have mostly relied on a large scale setup with bulk optical elements (such as beamsplitters and mirrors) bolted to room-sized optical tables, with photons propagating through air. In addition, single-photon qubit approaches have relied on unscalable single-photon sources and detectors. For both single photon and bright CV (continuous variables) approaches, there is now the need to develop high performance sources, detectors, and optical circuits that integrated on a single optical chip. For single-photon approaches it is also desirable to realize a strong optical nonlinearity at the single photon level, whereas for CV approaches an integrated high-bandwidth squeezer is desirable. There are already important examples, including photonic quantum circuits on a silicon chip [28], high-efficiency photon-number-resolving detectors [29], semiconductor-cavity–quantum-dot single-photon sources [30] and photonic crystal quantum-dot-based single-photon nonlinearities [31].

The need to integrate QKD into these nano-satellites and into novel applications gave rise to the miniaturization of devices for free space quantum key distribution [32, 33]. Integration of controlled phase shifters in integrated interferometers has been used to control single-photon qubit states, manipulate multi-photon entangled states of up to four photons and demonstrate on-chip quantum metrology [34]. An integrated quantum optical circuit comprising several one- and two-qubit gates was recently used to perform a compiled version of Shor's quantum factoring algorithm on a chip [35].

However, an efficient route to high-speed encoding of the quantum phase states on chip is still missing. In [36], a novel approach to high-speed phase encoding is exploited and a compact, scalable and power efficient integrated quantum transmitter is showed. A secure key rate of 270 kHz is achieved with a chip size of 6x2 mm^2.

An alternative fabrication technique based on direct laser writing has been demonstrated [37]. It

promises rapid prototyping, fabrication of high-density three-dimensional devices in material systems that do not lend themselves to conventional lithography, and also provides impressive control over the transverse spatial mode, which is important for low-loss coupling to sources and detectors. A hybrid fabrication approach using direct writing with UV lasers has also been showed [38]. Several challenges remain to be addressed, including low-loss interfacing with sources, detectors and optical nonlinearities, further miniaturization, fast switching and reconfigurable circuits.

In [39], an optical architecture of 35x20x8 mm^3 is proposed. In this work the polarization is controlled for each diode's emission by a wire-grid polariser and the spatial overlap accomplished by a femtosecond fabricated device. Tests with a free-space receiver showed an average error ratio of 3.3 % and an asymptotic secure key rate of 54 kHz under static alignment.

For now, no-one knows exactly how the future quantum technologies will look. It seems probable that quantum information will be transmitted in quantum states of light, and that some level of information processing will be performed on these states. Then, it also seems clear that developments in conventional photonics and integrated photonics must be realized in order to exploit the full potential of such technologies.

1.3 Thesis Overview

This thesis reports on the design of an integrated photonic circuit capable of implementing BB84-like protocols and a brief study of a PPKTP crystal recently acquired. To achieve a limited footprint and a low power consumption of the optical module, a novel architecture based mostly on passive components is designed. The use of femtosecond laser fabrication is evaluated and characterized. The proposed design and fabrication process were not tested due to limitations.

Chapter 2 presents a theoretical introduction to QKD and, in more detail, the implemented QKD protocol. It also discusses the technical challenges associated with implementing a quantum network. The use of satellites is considered. Finally, the current QKD system is shown and explained.

Chapter 3 deals with the fabrication process of integrated photonic waveguides using femtosecond laser fabrication. Various parameters are evaluated in order to find possible regimes for a functional application of this technique. The technique is assessed according to its advantages and disadvantages.

Chapter 4 focuses on the design and analysis of passive photonic components that can reproduce the same results as conventional bulk optic components. Then, the integrated photonic design is proposed and studied.

In chapter 5, the study of the spontaneous parametric down-conversion process and its uses is performed. Simulations are done in order to better understand the phenomenon and characterization of optical elements is presented.

All of the gathered results are summarized in the final chapter, which ends with an outlook.

Chapter 2

Quantum Key Distribution - From protocols to systems

Quantum Key Distribution protocols have attracted a lot of attention since their first proposal in 1984 [40]. QKD is a secure communication method which implements a cryptography protocol making use of principles of quantum physics. It enables two parties to produce a shared random secret key known only to them, which can then encrypt and decrypt messages.

The unique properties of QKD come from fundamental aspects of quantum mechanics as opposed to traditional public key cryptography, which relies on the computational difficulty of certain mathematical functions, and cannot provide any mathematical proof as to the actual complexity of reversing the one-way functions used. QKD has provable security based on information theory and forward secrecy.

One of its most powerful properties is that it can detect third party eavesdropping. If the level of eavesdropping is below a certain threshold, a key can be produced that is guaranteed to be secure.

Quantum key distribution is only used to produce and distribute a key, not to transmit any message data. This key can then be used with any chosen encryption algorithm to encrypt (and decrypt) a message which can then be transmitted over a standard communication channel.

2.1 The quantum mechanics of quantum communication

Quantum communication uses quantum bits, qubits, to encode and share information. Unlike classical bits, the qubit cannot only take the values 0 or 1 but can be in any superposition of the states $|0\rangle$ and $|1\rangle$. Mathematically this can be expressed by,

$$|\psi\rangle = \alpha\,|0\rangle + \beta\,|1\rangle \quad \alpha, \beta \in \mathbb{C}, \tag{2.1}$$

where $|\alpha|^2 + |\beta|^2 = 1$, $|0\rangle$ and $|1\rangle$ are orthonormal states and $|\psi\rangle$ is the state of the qubit.

The Bloch sphere, figure 2.1, is a geometrical representation of a qubit and can be a helpful tool to visualise states and operations on these. Any state can be represented in this sphere by a vector. The

antipodal points correspond to a pair of mutually orthogonal state vectors. While arbitrary, the north and south poles of the Bloch sphere are typically chosen to correspond to the standard basis vectors $|0\rangle$ and $|1\rangle$. The other poles correspond to different orthogonal basis.

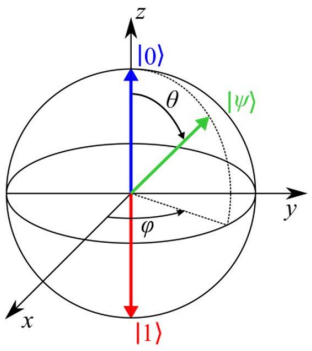

Figure 2.1: Bloch sphere representation of a qubit. [41]

In principle, any two-level system can be used as a qubit. In practice, these can be realized using different platforms like ion traps, atoms, spins and photons. Usually, photons are used for communication since they can be generated, controlled, and manipulated with rather simple linear optical devices. Furthermore, since photons rarely exhibit interaction with the environment, they are the best candidates for long-distance free space transmission as would be required in a future global network.

As further advantage, they offer the possibility to encode information onto different Degrees Of Freedom (DOF), such as the polarization, the orbital angular momentum (OAM), the frequency, time bins or the spatial mode.

As the atmosphere is practically non-birefringent, there is preservation of the polarization state during the free space transmission. Because of this and to the fact that the polarization can be manipulated with simple devices, throughout this work, it is used to encode qubits.

As light is a transverse electromagnetic wave, it has a polarization related to the geometrical orientation of the oscillations. By convention, the polarization of electromagnetic waves refers to the direction of the electric field. In linear polarization, the field oscillates in a single direction. In circular or elliptical polarization, the field rotates at a constant rate in a plane as the wave travels. The Poincaré sphere illustrates how all the polarizations states of a photon can be mapped into a sphere, showing a direct relation with the Bloch sphere, where every quantum state could be mapped into a sphere.

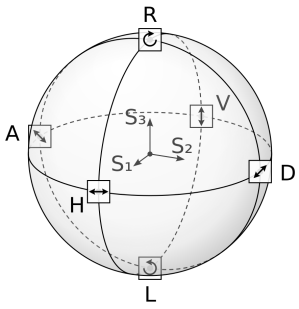

Figure 2.2: Drawing of a Poincaré sphere, which illustrates the space of possible polarizations of electromagnetic waves. [42]

What this means is, the state of the qubit can be the polarization of the photon. By convention, the horizontal polarization ($|H\rangle$) is defined as the $|0\rangle$ state and the vertical polarization ($|V\rangle$) as the $|1\rangle$ state. Any polarization can be given by a superposition of these two, as any state was the superposition of $|0\rangle$ and $|1\rangle$. This basis is the standard basis Z=$|H\rangle$,$|V\rangle$ but the qubits can also be written in other common basis such as X=$|D\rangle$,$|A\rangle$ and Y=$|R\rangle$,$|L\rangle$.

Basis	State	Linear polarization	Bit value
Z	$\|H\rangle$	0°	0
	$\|V\rangle$	90°	1
X	$\|D\rangle = \frac{1}{\sqrt{2}}(\|H\rangle + \|V\rangle)$	45°	0
	$\|A\rangle = \frac{1}{\sqrt{2}}(\|H\rangle - \|V\rangle)$	-45°	1
Y	$\|R\rangle = \frac{1}{\sqrt{2}}(\|H\rangle + i\,\|V\rangle)$	-	0
	$\|L\rangle = \frac{1}{\sqrt{2}}(\|H\rangle - i\,\|V\rangle)$	-	1

Table 2.1: Definition of the information stored in the polarization of a photon. $|D\rangle$ correspond to the diagonal polarization, $|A\rangle$ to the anti-diagonal polarization, $|R\rangle$ to the right circular polarization and $|L\rangle$ to the left circular polarization.

In order to access the information stored in the qubit, one has to measure it. When making a measurement, a basis must be chosen. The result will be one of the states that generates that basis. This is an important result from quantum mechanics.

Since the state of the qubit might not be one of the states of the basis chosen, the result is probabilistic in nature. For example, if the initial state is the diagonal polarization, $|D\rangle$, and the basis chosen is the Z basis, the probability of measuring an horizontal polarization, $|H\rangle$, corresponding to a bit value of 0 is given by:

$$P(|H\rangle) = |\langle D|H\rangle|^2 = \left|\frac{1}{\sqrt{2}}\left(\langle H| + \langle V|\right)|H\rangle\right|^2 = \left|\frac{1}{\sqrt{2}}(\langle H|H\rangle + \langle V|H\rangle)\right|^2 = \left|\frac{1}{\sqrt{2}}(1+0)\right|^2 = \frac{1}{2}. \quad (2.2)$$

This result means that there is a 50% chance of measuring a 0 and, therefore, a 50% chance of measuring a 1 if the measurement is made in Z basis and the state was in the diagonal polarization. After the measurement, the photon will be in the state measured, either horizontal or vertical polarization.

The probabilistic nature of the measurement might seem detrimental but actually, this propriety, in addition to the fact that, it is impossible to clone an unknown state, is the foundation of some QKD protocols. This will become clear in the following example.

2.2 QKD examples

BB84 Protocol

The BB84 protocol is one of the most widely used and simple QKD protocols. In an ideal world (perfect equipment and no undesirable interactions with the environment), it has been mathematically proven to be secure against all classical and quantum attacks [43], as have other QKD protocols. In addition, Alice and Bob can detect any attempt by an eavesdropper (E)ve to eavesdrop on the key distribution process.

Any type of communication is made between at least two parties, Alice and Bob in this case. In order to implement the BB84 protocol, Alice and Bob need to share a classical public communication channel and a quantum communication channel. A quantum channel is nothing more than a channel that can transmit qubits. This could be, for example, an optical fiber or even free space. The steps of the protocol are:

1. Alice begins by choosing a random string of bits

2. For each bit, a basis is randomly chosen between Z and X

3. Alice transmits each qubit to Bob over the quantum channel

4. Bob randomly chooses a basis in which to measure each qubit (Z or X basis)

5. Bob and Alice notify each other over any classical channel (even insecure ones) what basis they used to measure each qubit

6. Alice and Bob will discard the bits corresponding to the qubits measured in different basis

7. Alice and Bob should now have an identical string of random bits which is called a sifted key

The results measured in a different basis to that in which they were created are discarded because they cannot be predicted to be correct. If Alice sends a photon with an horizontal polarization and thus a bit with value 0, Bob can measure either diagonal or anti-diagonal polarization if he chooses to measure in the X basis. The probability will, in theory, be 50% of getting the correct result. Otherwise, when Bob chooses the same basis as Alice, the probability of measuring the correct bit value is 100%. Therefore, these measurements are kept as they will result in the creation of the sifted key. As the probability of Bob choosing the same basis as Alice is 50%, only half of the bits sent will not be discarded, on average.

Alice's bit	0	1	1	0	0	0	1	1
Alice's base	Z	Z	Z	Z	X	X	X	X
Alice's polarization	0°	90°	90°	0°	45°	45°	-45°	-45°
Bob's base	Z	X	Z	X	X	Z	Z	X
Bob's measurement	0°	45°	90°	45°	45°	0°	90°	-45°
Matching basis	✓	×	✓	×	✓	×	×	✓
Shared secret key	0		1		0			1

Table 2.2: Possible outcomes of the BB84 protocol. In the end, only half the bits are kept and used to create the sifted key.

This is the ideal scenario. No noise (change in the state during the transmission) was considered and more importantly, no attacker. To understand why the BB84 protocol is provably secure, an analysis of third parties attacks has to be made.

Assuming that the receiver and sender are secure and that all the steps are performed perfectly (all the components are ideal and perform as in theory), Eve, the attacker, can only interfere with the transmission of information (step 3 or step 5). Through the public classical channel, she has access to the basis used but she cannot gather any information about the bit's value through that. She does not know what Bob actually measured. The only option is through the information shared over the quantum channel.

Due to the no-cloning theorem, Eve cannot intercept, copy and resend the qubit unchanged to Bob. If Eve intercepts the qubit and tries to find any information about it, she has to measure it. Even assuming Eve has access to all technology allowed by the laws of physics, she has to choose a basis in which to measure. If she makes the right choice, the measurement will correspond to what Alice sent and she can resend the qubit to Bob unchanged. If the basis are not the same, then she has a 50% chance of measuring the correct value, as Bob did. However, she will now have changed the qubit that Alice sent, causing an error to appear on Bob's side.

For example, Alice sends an horizontally polarized photon. If Eve chooses the Z basis she will measure a horizontally polarized photon and resend that. If she chooses the X basis, she will either measure a diagonally or anti-diagonally polarized photon and resend that which she measured. In this case, even if she gets the right bit value by chance, she will have changed the qubit directed to Bob. This can be seen in table 2.3.

Bit sent	Alice's basis	Eve's basis	Polarization sent by Eve	Bob's basis	Bit measured by Bob
0	Z	X	-45°	Z	1

Table 2.3: Example of possible bit error induced by the presence of Eve.

As Eve has no more information than Bob, the best option is for her to randomly choose a basis in which to measure. This means she will get the correct basis 50% of the time and alter the qubit the other

50%. Bob will then start to have some errors in his measurements.

This means that if Alice and Bob share part of the key they have, they can find Eve by calculating the bit error rate, BER. The BER is the percentage of wrong bits in a shared key. The interference of Eve in the way described previously creates a bit error rate of at least 1/4. However, there exist more refined attacks than resulting in lower BER, most notably the phase-covariant cloning machine with a BER of 14.6% [44].

As the BER is not only influenced by the eavesdropper's strategies, but also by the imperfections of the physical devices and the channel through which the quantum states propagate, a threshold must be defined. If the measured BER is higher than this threshold, the communication is stopped. This value is chosen in order to maximize the transmission rate while minimizing the probability of Eve extracting information. The objective is for Eve to not get enough information to find the key. Sometimes and with some privacy amplifying protocols, Eve can be allowed to get information until a certain point with minimal risk. Moreover, studies of the noise from various known source can be made to subtract it from the total BER and have a better parameter to estimate possible attacks.

The method described before is the simplest type of possible attack, intercept-resend attack. However, as stated before, Eve can use other methods to try to acquire information. Common attacks include the photon number splitting attack, taking advantage of the source not being a true single photon emitter, man-in-the-middle attack, in which Alice mistakes Eve for Bob due to Alice and Bob not having authenticate each other and established a secure connection and trojan-horse attack. Nevertheless, even with unlimited resources and thus more possible attacks, this protocol is secure as long as: Eve cannot physically access Alice and Bob's encoding and decoding devices; The random number generators used by Alice and Bob is trusted and truly random; The classical communication channel is authenticated using an unconditionally secure authentication scheme; The message is encrypted using one-time pad like scheme;

Finally error correction is applied to the remaining sifted key. In it, Alice and Bob apply classical error-correcting algorithms to remedy the effect of random errors caused by channel noise and by the fact that equipment is non-ideal.

E91 protocol

The BB84 protocol was an example of a prepare and measure protocol. In general, measuring an unknown quantum state changes that state in some way. This can be used to calculate the amount of information that has been intercepted. These are not the only category of QKD protocols.

One major propriety of quantum mechanics not discussed yet is entanglement. A pair or group of particles is said to be entangled when the quantum state of each particle of the pair or group cannot be described independently of the state of the others, including when the particles are separated by a large distance.

In entanglement based protocols, a entangled pair of objects is shared between two parties and anyone intercepting either object alters the overall system, revealing the presence of the third party (and the amount of information they have gained). This happens because the quantum states of two (or more)

separate objects become linked together in such a way that they must be described by a combined quantum state, not as individual objects.

The E91 protocol can be implemented using photon pairs generated by Alice, Bob or by some source separate from both of them, including eavesdropper Eve. The pair is distributed to Alice and Bob, each keeping a photon from the pair. It is assumed the entangled states are perfectly correlated. This means that if Alice and Bob measure the photon's orientation in the same basis they will always obtain opposite responses, independent of the basis chosen. The individual results are completely random, meaning that Alice's measurement cannot be predicted, for instance, a vertical or horizontal orientation. On the other hand, any attempt to listen made by the Eve will ruin the correlation, which can be detected by Alice and Bob.

The measurement stage involves Alice measuring each photon she receives using some basis from the set $Z_0, Z_{\frac{\pi}{4}}, Z_{\frac{\pi}{8}}$ while Bob chooses from $Z_0, Z_{\frac{\pi}{4}}, Z_{\frac{3\pi}{8}}$ where Z_θ is the Z basis rotated by θ. The steps of the protocol are then as follows:

1. N pairs of entangled states are generated in a random way
2. For each pair of entangled state, one is sent to Alice and another to Bob
3. Alice and Bob independent and randomly choose a measure basis from their set and apply them to each photon
4. Bob and Alice notify each other over any classical channel (even insecure ones) what basis they used to measure each photon
5. The first group of photons is created from the measurements using the same basis by Alice and Bob
6. The remaining measurements are the second group
7. Using the second group, they calculate the test statistic S
8. If S does not reveal the presence of Eve, the first group of photons is used as the secured key

For each selected value of θ_A and θ_B, the numbers of coincidences in each category $(N_{++}, N_{--}, N_{+-}, N_{-+})$ are recorded. The experimental estimate for E(θ_A, θ_B) is then calculated as:

$$E = (N_{++} + N_{--} - N_{+-} - N_{-+}) / (N_{++} + N_{--} + N_{+-} + N_{-+}). \tag{2.3}$$

Once all four E's have been estimated, an experimental estimate of the test statistic can be made:

$$S = E\left(0, \frac{\pi}{8}\right) - E\left(0, \frac{3\pi}{8}\right) + E\left(\frac{\pi}{4}, \frac{\pi}{8}\right) + E\left(\frac{\pi}{4}, \frac{3\pi}{8}\right). \tag{2.4}$$

Maximally entangled photons would result in $S = 2\sqrt{2}$. If this is not the case, then Alice and Bob can conclude something has introduced local realism to the system, something has reduced the about of entanglement in the system. This does not mean there is an attacker. Interactions with the environment could have decreased the value of S. As in the BB84, a threshold must be decided upon. An estimation on

how much information a possible attacker could have extracted can be computed from S and the decision of aborting or continuing the protocol can be made. If the protocol is successful, the first group can be used to generate keys since those photons are completely anti-aligned between Alice and Bob.

These two approaches can each be further divided into two families of protocols: discrete variable and continuous variable. Discrete variable protocols were the first to be invented, and they remain the most widely implemented. CV protocols are mainly concerned with overcoming practical limitations of experiments. In this work, only DV protocols are explored.

2.3 Implementation aspects

Security of a QKD key is always a quantitative affair because of non-ideal equipment and channel noise, so some non-trivial information might be picked-up by Eve without being detected during the communication. However, the amount of leaked information can be guaranteed to be below a certain threshold. Therefore, privacy amplification can negate the knowledge about the final key. This means the value of BER is chosen as a compromise between the amount of information Eve may have and the value that maximizes the number of bits transferred.

In order to implement QKD protocols in real life, an experimental setup has to be designed and characterized. As photons are the carriers of information, this setup has to have a photonic circuit, a way to create, manipulate and detect these photons. This is the hardware-intensive portion of the protocol, for which good random-number generators, single-photon sources, and single-photon detectors are required. This module has to be connected to an electronic module in order to control and read the photonic circuit.

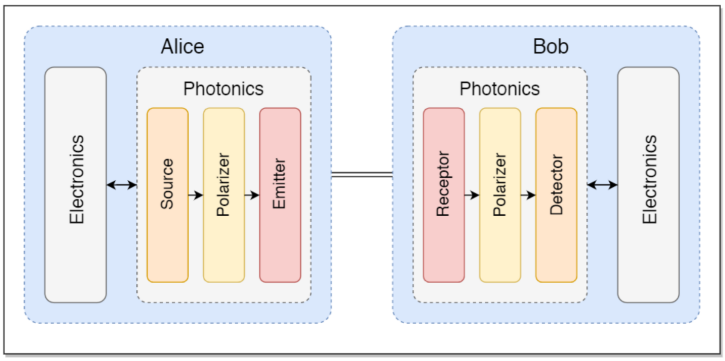

Figure 2.3: Schematic of a general QKD setup

Figure 2.3 shows the general design of a QKD system. The specifications of each module have to be chosen according to the objective in mind. For example, in order for this communication system to compete with classical communication devices, it should run at 100 MHz in order to guarantee high key generation rates, exceeding 10^6 sifted bits within a few seconds. If the secret key rate is smaller, it may not be feasible to encrypt common messages. The choice of components also depends on how the transmission is implemented, either free-space or over optical fibers.

Photons can be manipulated by standard bulk optics, and their detection can be performed rather

efficiently over a wide wavelength range. For this reason, most proof-of-concept QKD experiments are done with bulk optics. However, the use of commercial mirrors and beam splitters to construct the optical circuit, usually leads to a large footprint. Because of this, real life applications and wide-scale deployment in optical networks will benefit from an optical platform that allows miniature devices capable of encoding the complex signals at high rates and with low power consumption.

The most common approach in the literature is photonic integration. It is the ideal route toward miniaturisation. However, an efficient route to high-speed encoding of the quantum phase states on chip is still missing. In [36], a novel approach to high-speed phase encoding is exploited and they show a compact, scalable and power efficient integrated quantum transmitter.

A secure key rate of 270 kHz was achieved with a chip size of 6x2 mm^2.

In [39], an optical architecture of 35x20x8 mm^3 is proposed. In this work the polarization is controlled for each diode's emission by a wire-grid polariser. The beams are then spatially overlapped in a polarisation-insensitive femtosecond laser written waveguide array, and combined with a red beacon laser using an external beamsplitter to ensure a stable, synchronised optical link with the receiver. Tests with a free-space receiver showed an average error ratio of 3.3 % and an asymptotic secure key rate of 54 kHz under static alignment.

The approach presented in this papers follows from this work but tries to integrate the control of the polarization in the femtosecond laser written device.

2.4 Spatial mode mixing with bulk optical components

Different QKD protocols have been implemented using bulk optics in recent times. In 2019, the telecommunication institute of Portugal performed the first quantum communication experiment in the country using free-space propagation with a bulk optics approach.

This experiment was a success. Nevertheless, in order to achieve better results and more practical applications, new ideas are being explored.

For now, only the optical part of the experiment is analyzed and the protocol chosen is the BB84. As this is one of the simplest QKD protocols, it is excellent for proof-of-concept experiments.

In order to implement the BB84 protocol, an emitter and a receiver are necessary. The emitter, Alice, has to be able to deterministically prepare one of four polarized states. These four states are, in this case, the horizontally polarized ($|H>$), the vertically polarized ($|V>$), the diagonally polarized ($|D>$) and the anti-diagonally polarized ($|A>$). The Jones matrix corresponding to each state can be seen in table 4.1.

The receiver must be able to detect the polarization of the incoming photon. This detection can be flawed in theory, as explained previously. Nevertheless, the receiver should be able to perform a detection for every photon received as the protocol dictates.

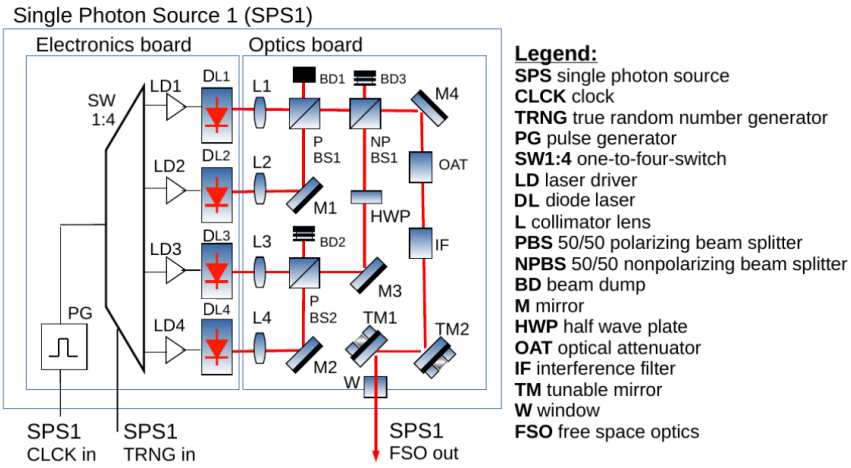

Figure 2.4: Schematic of the emitter (Alice) used for the BB84

In figure 2.4, a design for an emitter using bulk optics is presented. It can be seen that there are four inputs and one output. Each input is connected to the output through a different optical path, through different optical elements. These guarantee that each path has a different and determined polarization at the output. Therefore, by switching on only one of the diode lasers at each emission, one of the four polarized states is created at the output.

For example, if the string of states $\{|H>,|H>,|V>,|A>\}$ was to be emitted, one would only have to switch on the diodes lasers in the order $\{1,1,2,4\}$ respectively.

The diode lasers used here are not single photon sources, however, using filters to attenuate the intensity, weak coherent pulses are created. The average pulse rate can be controlled and is chosen in order to have one photon in most pulses while minimizing the likelihood of having two photons, as emitting two photons leaves the protocol open to different attacks (e.g. photon number splitting attack). While there are no perfect single photon emitters, there are better approaches. This one is used here for it suffices for proof-of-concept tests and it is cost/efficient. A possible better source of single photons is studied later.

The design for the receiver is not shown, however, it is very similar to the emitter. The output becomes the input and the inputs are now outputs. This means a photon enters the receiver and is directed through an optical path to the detectors that now replace the diode lasers. Because of the nature of the protocol, two identically polarized photons can end up travelling different paths and signalling different detectors. This is part of the protocol and not a problem with the setup. The rest of the optical elements are the same and in the same locations.

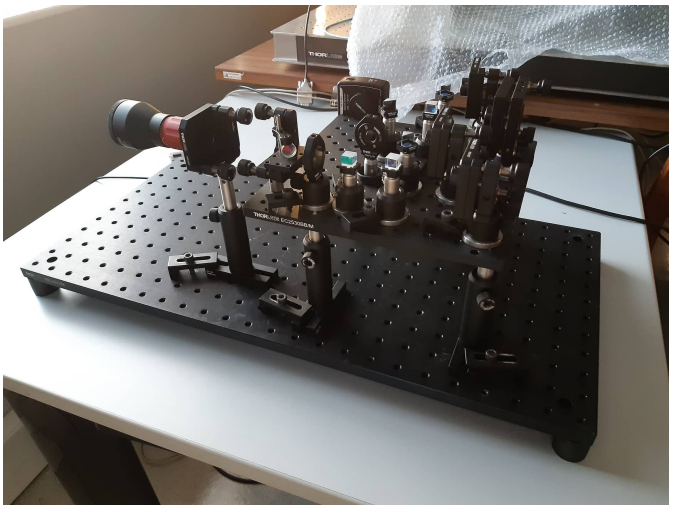

Figure 2.5: Optical setup of the emitter (Alice) used for the BB84 protocol.

Figure 2.5 shows the optical part of the emitter assembled in the lab. As it can be seen, it is too big and heavy for practical applications. Most of the size comes from the optical part of the setup (shown in the figure) while the electronics (not shown in the figure) can already be made to fit the requirements of small-scale applications.

2.5 Secure networking on intercontinental scales - the need for satellite based QKD

QKD networks have been studied and developed around the world in the past decades, which mainly comprises laying down fibers as the basic transmission medium to serve security demands with secret-key provisioning [45, 46]. The construction of QKD backbones and metro-area networks currently has been launched with enormous investment, and their development is attracting great attention around the world. Nevertheless, traditional QKD is limited to point-to-point connectivity.

While point-to-point connectivity is a necessary step in a network, a fully functional communication network cannot be built solely on these. It would not be possible to enable the access to many users and also to extend the reach and geographical coverage. Other methods must be devised and studied.

The first and the simplest approach is to use trusted relays. This is already feasible with current technology, and it has been used as the standard in existing QKD networks [47]. By setting up a trusted node, to relay secrets, it is possible to achieve secure communication over arbitrarily long distances. The problem with this method is that it relies on the security of the nodes. This is an extra security step on implementing a protocol to improve security. And while some trusted nodes would be feasible, if global coverage is the aim, many nodes would be necessary as the distance between each other would be small (50-100 km for example). This represents a remarkable security flaw, as an attack on a node could damage the entire network.

This problem could be solved if there was no need to trust the node. However, quantum repeaters are beyond current technology, but have been a subject of intense research efforts in recent years. There

is currently no way to resend qubits without measuring them, hence, trust has to be put on the nodes.

The solution then has to rely on trusted relays. The problems associated with these can be reduced by decreasing the number of nodes. A good approach to this is SatQKD. It would be possible to extend the distance of secure QKD to the global scale. Nevertheless, the use of optical fibers is restricted. To accomplish this, free-space transmission must be used.

The creation of constellations of QKD satellites can bring closer a large scale or even global quantum network that enables the sharing of symmetric encryption keys between any two points on Earth. In [48], a constellation model is described which enables QKD-derived encryption keys to be established between any two ground stations with low latency. One approach to achieve this result is to use nano-satellites (wet mass from 1 to 10 kg). This will not only increase the accuracy and precision of the satellites but also improve cost-efficiency when the capabilities of nano-satellites are advanced. Reducing satellite size without compromising accuracy hence reduces the cost of a single satellite, and increases the possibility of launching many satellites, enabling the improvement of the spatio-temporal coverage of satellite constellations.

There are still technical questions and problems to be solved in order to advance with this idea. One of these and the one explored in this work is the miniaturization of the quantum payload, while keeping its efficiency.

Chapter 3

Analysis of femtosecond laser fabrication for integrated photonic waveguides

Commonly, high density optical circuit fabrication is done using conventional technologies readily integrated with standard CMOS fabrication techniques [49, 50]. These fabrication techniques place some limitations on circuit design. Large-scale production design can be completed in several ways, but in order to produce waveguide patterns either a chrome mask to selectively illuminate a photosensitive resist or electron beam lithography is needed. This restricts the flexibility of the circuits.

The femtosecond laser direct-write technique is a unique way to produce glass waveguides. In recent years, femtosecond (fs) laser direct writing of transparent material has become a powerful microfabrication technique for passive and active integrated optical devices. The capability to create three-dimensional complex optical waveguide circuits has opened up new opportunities for integrated photonics. The ability to create 3D optical or photonic devices by sequential direct-writing of individual devices can lead to more flexible, efficient and smaller quantum circuits.

The waveguides formed through femtosecond laser direct write (FLDW) can be fabricated with a refractive index contrast and diameter closely resembling an optical fiber meaning that insertion losses are minimal. This means that typical waveguides can still be used for the output and input if necessary.

The structure produced depends on laser parameters (pulse duration, wavelength, energy, repetition rate), material parameters (band gap, thermal expansion coefficient, etc.), and the numerical aperture (NA) of the focusing.

3.1 Background

When a femtosecond laser pulse is focused inside a transparent material, the optical intensity in the focal volume can become high enough to induce permanent structural modifications such as a refractive index

change or the formation of a small vacancy.

This effect results from nonlinear absorption processes. The incident photons do not have enough energy to overcome the band gap energy of the dielectric materials. However, when the incident laser intensity is high enough, nonlinear optical effects are observed. The first is photoionization.

Photoionization is the direct excitation of the electrons by the laser. It can happen as a result of two different interactions, depending on the characteristics of the laser pulse. For low laser frequencies and strong laser fields, Tunnelling Ionisation is often observed. In this regime, the band structure of the dielectric can be distorted by the strong electromagnetic field and band-to-band transitions occur, electrons tunnel out of the valence band and become free electrons. If the laser pulses have a high repetition rate, Multi-photon Ionisation (MPI) is more likely to happen. MPI occurs when the material absorbs over one photon. The number of photons it needs to absorb is calculated by $N \cdot hf > E_g$. In silica it is usually at least 6 photons [51]. These processes can be observed in figure 3.1

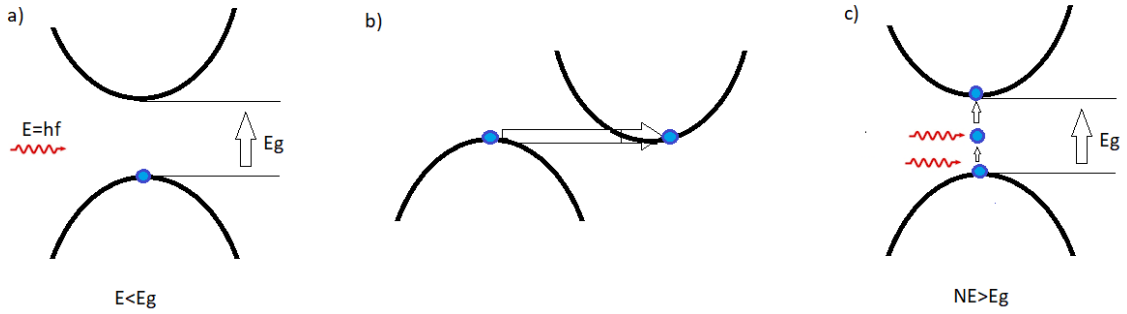

Figure 3.1: Schematic representation of nonlinear photoionisation processes underlying femtosecond laser machining. (a) No photoionisation, (b) Tunnelling Ionisation (c) Multi-photon Ionisation

After the photoionization process, there are some free electrons in the material. These electrons keep absorbing energy from the laser pulse and avalanche ionization occurs. The energetic free electrons have enough energy to excite the valence electrons to the conduction band, giving rise to more free electrons. This results in an exponential increase in the number of free electrons.

This creation of an electron gas occurs on a time scale below the time scale of energy transfer within the system. Because of that, the two processes can be addressed separately. A femtosecond laser pulse produces a strong nonequilibrium condition in a material with electron temperatures much higher than lattice temperatures. The result of the femtosecond laser on the material will then be the way the systems react to the nonequilibrium condition.

For a more detailed explanation, [52–54] are suggested.

3.2 Modification regimes induced by laser intensity

To date, three qualitatively different structural changes have been induced in the bulk of transparent materials with femtosecond laser pulses. These modifications are characterized by the intensity of the

laser and by the material properties. This can be seen in figure 3.2.

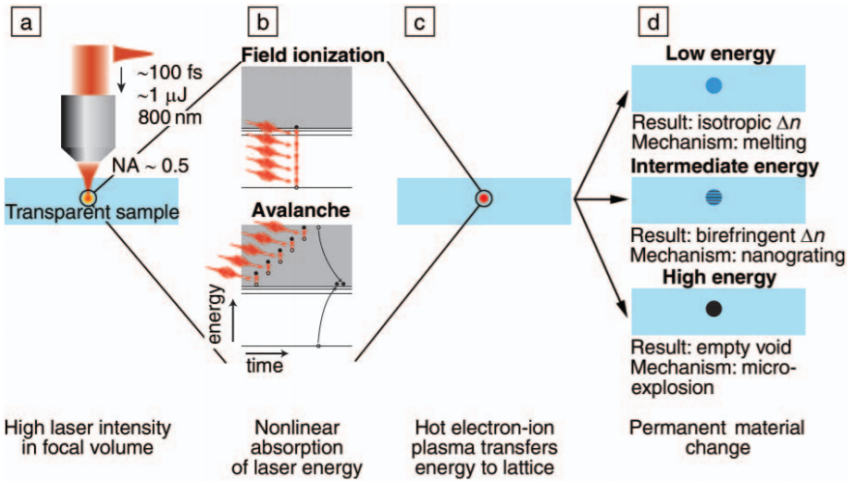

Figure 3.2: Schematic illustration of key steps in femtosecond-laser-induced structural change in bulk transparent materials [55]

Smooth Refractive Index Change

This type of modification, also known as Type I, is ideal for low loss waveguides. The refractive index of the material suffers an isotropic change on the focus spot of the laser. The reason behind this change is not fully understood, but it is possible a combination of three different mechanisms.

The energy deposited on the focal volume of the material leads to rapid heating and change in the material [56]. As this change is concentrated on very small volume of the material, it cools very rapidly. Infused silica, the density increases if the glass is quenched from a high temperature, explaining the higher refractive index (typically on the order of 10^{-3}) observed in femtosecond laser irradiated fused silica [57, 58].

The production of colour centres by the radiation has also been showed to affect the refractive index by various groups [59–61]. The high electron density, produced by the nonlinear absorption mechanisms outlined above, lead to a sufficient trapped species (colour centres) concentration in the exposed region resulting in different substrate defects being formed. However, if this effect is eliminated by annealing (photobleaching), the refractive index does not return to normal [62].

Poumellec et al. [63] showed that densification and strain in the glass because of femtosecond laser radiation may also account for changes in the index of refraction. Raman microspectroscopy measurements show an increase in the number of 3- and 4- member ring structures in the silica network following femtosecond laser irradiation, while 5- and 6-member rings predominate in untreated glass. This increase in the number of smaller rings is consistent with densification [64]. It has also been shown that the refractive index and the abundance of these low rank ring structures in femtosecond laser exposed regions increase in the same way.

None of these effects alone can justify the change in the refractive index, it is most likely due to a

contribution of all of them.

Birefringent Refractive Index Change

At intermediate intensities, a non-isotropic index change has been observed, resulting in birefringence and negative refractive index change. This means the waveguides support guided modes with different propagation constants for two orthogonal polarization states. This allows to fabricate waveguide segments acting as integrated waveplates or even more complex designs due to interaction between birefringent waveguides.

The appearance of birefringence can result from diverse effects, depending on the substrate material and the irradiation conditions. For example, the ellipticity of the waveguide cross-section, mechanical stress in the modified region or laser-induced intrinsic birefringence aligned according to the writing beam polarization.

With laser-induced intrinsic birefringence, nanostructures can be observed. These are self-ordered and periodic (with a size and period as low as 20 nm and 140 nm respectively) while being orientated in a direction perpendicular to the electric field vector of a linearly polarised femtosecond laser writing beam [65]. The mechanism proposed to explain the formation of the nanogratings involves interference between the femtosecond laser field and the electric field of bulk electron plasma waves in the laser-produced plasma. This interference leads to periodic modulations in the electron plasma density, which leads to periodic modulations in the degree of structural change produced [66].

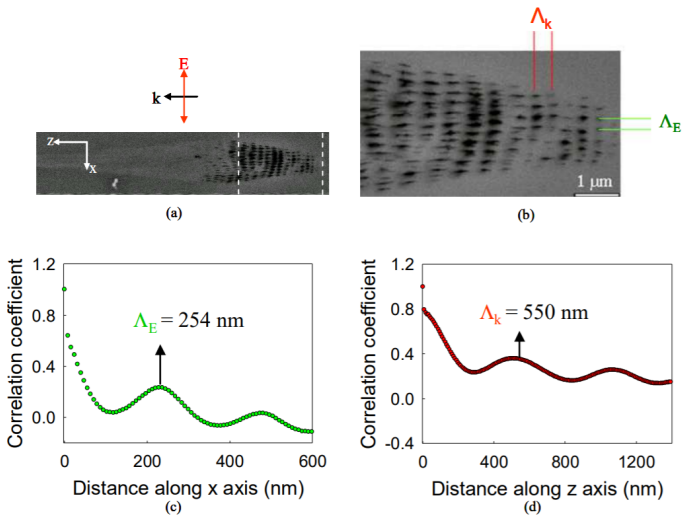

Figure 3.3: (a): SEM image of a written line in the xz plane, E: electric field of the writing laser, k: wave vector of the writing laser beam (λ = 800 nm, τ_p =150 fs, Ep = 0.5 μJ, V = 100 μm/s, Rep = 250 kHz). (b): The region between two dotted lines is used for calculation. Corresponding normalized correlation functions calculated along the x (c) and z (d) axis. [67]

A systematic study of the properties of nanostructures and their dependence on various irradiation parameters was performed in [67]. From their analysis in figure 3.3, two periodic structures can be

observed. Besides the main period Λ_E, which is in the polarization's direction of the laser beam (E), a second period Λ_k is identified perpendicular to Λ_E, and hence parallel the direction of propagation of the laser beam (k).

They found that that Λ_E decreases with increasing laser energy within the study range (0.1-2μJ). Results suggest that the period Λ_E is proportional to the wavelength of the writing laser, meaning, shorter wavelengths yield significantly smaller structures. These results are only for a certain range of values. The general behaviour might be different.

Self-assembled nanostructures, within the irradiated volume, are not the only method responsible for the femtosecond laser induced type-II modifications which are characterized by average negative index change and form birefringence.

Another way to create birefringent refractive index change is through stress. For stress birefringence, the relation between the retardance (R) and stress (σ) is defined as:

$$R = C_{pe} \cdot \sigma \cdot d, \tag{3.1}$$

where C_{pe} is the photoelastic coefficient, d is the thickness of the birefringent region. This implies that the stress is mainly induced from the light induced thermal expansion. This effect is observed and documented in [67]. An interesting propriety of stress induced birefringence is that the stress can be removed from glass by annealing at the transition temperature. Meaning that these changes can be erased if desired.

In addition, the stress can also be created using stress tracks as shown in [68]. This method can be seen in figure 3.4 and it has been used in other works as well [69–71].

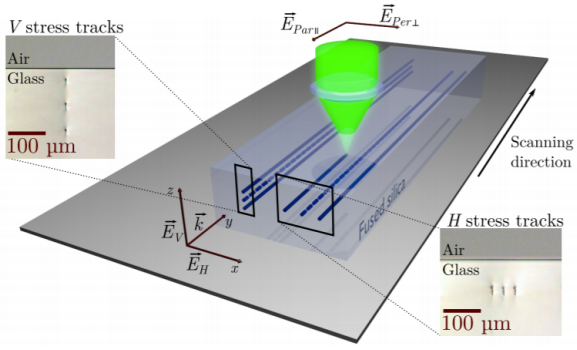

Figure 3.4: Schematic arrangement for the stressed waveguide fabrication where $\vec{E}_V$ and $\vec{E}_H$ indicate the electric field orientation for Vertical, V, and Horizontal, H, waveguide polarization eigenmodes, while $\vec{E}_{Par\parallel}$ and $\vec{E}_{Per\perp}$ represent the parallel and perpendicular polarizations of the writing laser, respectively. The insets show microscope end view images of the Bragg grating waveguides sandwiched with vertical (left) and horizontal (right) stress tracks. [68]

This process results not only in, at least, a 3-fold increase of the birefringence but also allows the tuning of this parameter. In [71] it is shown that through control of the relative position of the stress track, it is possible to have control over the fast and slow axis. All these properties allow for smaller

components created by femtosecond laser writing.

Finally, Roberto Osellame developed a simple technique to create a birefringent waveguide with tilted optical axis in [72]. A schematic design of this technique can be seen in figure 3.5.

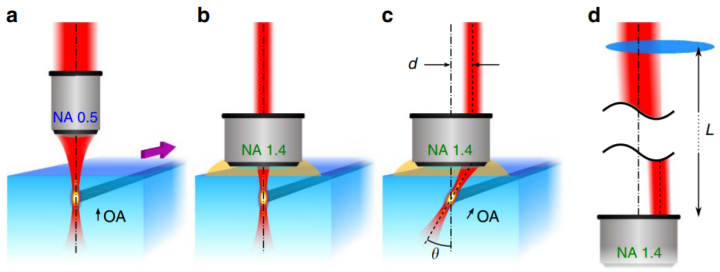

Figure 3.5: Conceptual scheme of the method enabling the direct writing of optical waveguides acting as integrated waveplates with tilted axis. (a) Traditional writing scheme adopting a focusing objective with moderate NA; the symmetry of the writing layout creates birefringent waveguides with the optical axis (OA) aligned as the writing beam direction; actual waveguide writing is performed by a transverse translation of the glass sample (indicated by the purple arrow). (b) Equivalent waveguides can be created by underfilling a high-NA oil-immersion objective. (c) Offsetting the writing beam before the objective results in waveguide writing with an inclined laser beam; the resulting waveguide has an optical axis tilted by an angle y that depends on the amount of offset d of the writing beam with respect to the objective axis. (d) Reduced beam size and offset at the objective aperture is achieved by a small transverse shift of a long focal lens placed at a distance L from the focusing objective.[72]

In the same work, it is shown how this technique can be applied to the creation of a integrated device for quantum tomography of a two-photon state. Moreover, in latter work, this same technique is used to experimentally show the fabrication by femtosecond laser micro-machining of components such as polarisation insensitive and polarising directional couplers [73].

All in all, there are various processes through which birefringent waveguides can be created and manipulated. This allows for a wide range of tuning of the required parameters and choice in the materials used.

Voids

When the laser intensity reaches critical values for the material, the region of modification is characterised by material damage or void formation. This is caused by an explosive expansion of highly excited, vaporized material out of the focal volume and into the surrounding material, a process called micro-explosion [74, 75]. This explosion or expansion occurs within the bulk of a material, the shock wave carries matter and energy away from the focal volume, compressing the surrounding material and leaving a rarified (less dense or hollow core) central region termed a void.

The contention that shock waves exist during femtosecond laser modification with high pulse energies is supported by the detection of acoustic or pressure waves originating from the focal point [76, 77]. Voids have been used in for the fabrication of optical memory devices and other devices not interesting for this work.

3.3 Modification regimes induced by the laser's repetition rate

Besides the modifications caused in the material due to the intensity of the laser, the repetition rate also creates distinct regimes when fabricating photonic circuits. This results from the overlap between the relaxation time of the material and the arrival of the next pulse, as can be seen in 3.6.

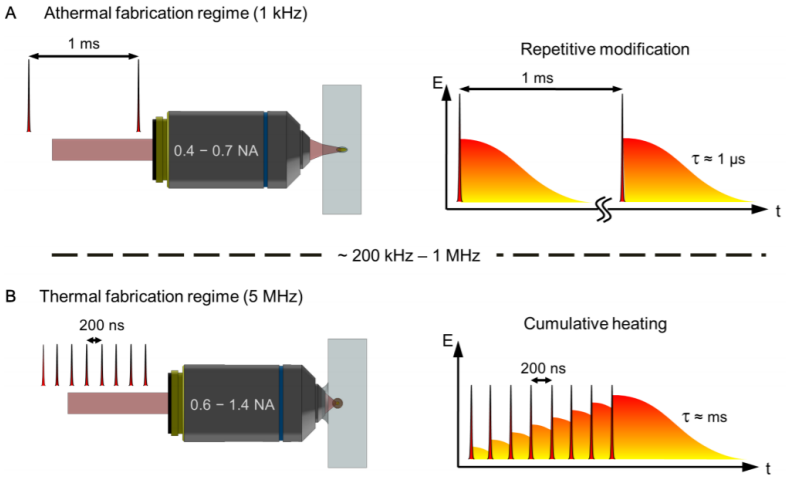

Figure 3.6: Schematic of the thermal regimes [78]

Athermal regime

In the athermal regime, where the time span between successive laser pulses is considerably longer than the thermal diffusion time of the glass, which is typically of the order of microseconds, a pulse-by-pulse repetitive modification of the material occurs. Because of the low pulse repetition rate (< 100 kHz), slow translation speeds, typically in the order of tens of micrometres per second, are required in order to achieve sufficient spatial overlap between individual modifications to create a continuous waveguide.

If a low NA objective (< 0.5 NA) is used with a low repetition rate for femtosecond laser, the focal volume (and hence the changed material volume) becomes asymmetric. As showed in [79], there are ways to overcome this problem but that result in more complex setups.

Thermal regime

In contrast, in the thermal regime, successive pulses arrive well below the thermal diffusion time of the material. Thus there is insufficient time between pulses for the heat to diffuse out of the focal volume and an accumulation of heat occurs. Because of the high laser repetition rate, the sample can be translated at speeds of millimetres per second, and thus the waveguide inscription is orders of magnitude quicker than in the athermal regime.

A volume of material much greater than the focal volume can be structurally altered, because if enough energy is absorbed, a volume of material larger than the focal volume can be heated above the melting temperature [80]. Also, because of symmetric thermal diffusion outside of the focal volume, a spherically shaped modified region is produced.

In conclusion, the thermal regime is more advantageous to create the devices necessary for photonic circuits. Nevertheless, the athermal regime can be adapted to produce similar results, but slower and with extra complexities.

3.4 Different writing configurations for waveguide inscription in glasses

In other to fabricate a waveguide or any other device using FLDW, the focal spot has to be moved through the material. Usually, the sample is placed on computer controlled motion control equipment to translate it in three dimensions regarding the focal spot. The sample can either be translated parallel to the laser beam direction, the so-called longitudinal writing, or perpendicular to the laser beam, transverse writing as illustrated in figure 3.7.

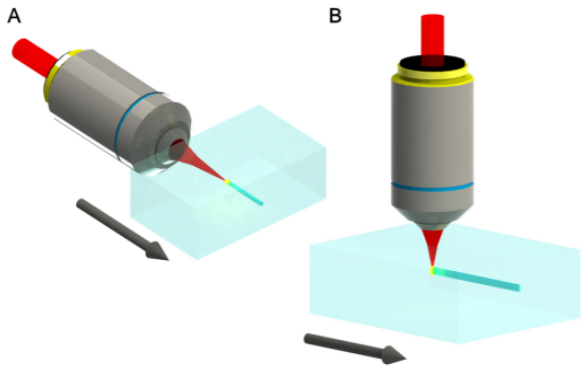

Figure 3.7: Schematic of inscription processes [78].

The longitudinal writing technique offers the advantage that the waveguides will be closer to circular in shape. However, the working distance of the objective lens limits the writing length of the waveguide. Thus, low-NA objectives with a long working distance

(the distance between the front lens of the objective and the point of focus) are needed to produce waveguides with a length of a few centimeters.

The transverse writing geometry is more flexible. Structures can be fabricated within the bulk material, limited in size only by the positioning system, while the maximum structure depth is determined by the working distance of the focusing objective. The major disadvantage, however, is the asymmetry of the produced structure. Except for very high-NA objectives, the focal radius will always be much smaller than the confocal parameter, resulting in a waveguide with an elliptical cross section. However there are techniques or conditions where this disadvantage can be mitigated.

All in all, the transverse writing scheme is preferred to the longitudinal one. It offers more flexibility when designing circuits and its disadvantages can be suppressed.

Chapter 4

Analysis and design of integrated waveguide based spatial mode mixing with polarization control for QKD

Photonic integrated circuits are devices on which several optical (and often also electronic) components are integrated. The technology of such devices is called integrated optics. Photonic integrated circuits are usually fabricated with a wafer-scale technology (involving lithography) on substrates of silicon, silica, or a nonlinear crystal material such as lithium niobate (LiNbO3). The substrate material already determines several features and limitations of the technology. This technology has a wide range of applications in areas from fiber-optic communication [81, 82], biological sensors [83] and quantum technologies [84, 85].

In this work, a novel approach is used to design the circuits (rather than lithography). The procedure is to use femtosecond laser fabrication to create the devices needed to make a photonic circuit. In addition, as the system should work without outside input, a passive design made of passive components is desirable.

This chapter will focus on the design, analysis and optimization of various passive components that may create the desired device. It starts by analyzing each building block used and then how they can be combined to create more complex components that can perform the necessary functions. Finally, a design is proposed and studied.

Unfortunately, there is no software that adequately handles polarization for the circuit simulations. A final design is proposed and using results found in the literature, an overall estimation of its functionality is done, as well as comparison with other similar devices.

4.1 Background

In optics, polarized light can be described using the Jones calculus. Polarized light is represented by a Jones vector, and linear optical elements are represented by Jones matrices. When light crosses an

optical element, the resulting polarization of the emerging light is found by taking the product of the Jones matrix of the optical element and the Jones vector of the incident light.

The Jones vector describes the polarization of light in free space or another homogeneous isotropic non-attenuating medium, where the light can be properly described as transverse waves. The polarization of the light can be determined by studying the electric field. The complex amplitude of the electric field is given by:

$$\mathbf{E} = \begin{bmatrix} \mathbf{E_x} \\ \mathbf{E_y} \\ \mathbf{E_z} \end{bmatrix} = \begin{bmatrix} E_x e^{i(\beta z - \omega t + \phi_x)} \\ E_y e^{i(\beta z - \omega t + \phi_y)} \\ 0 \end{bmatrix} = \begin{bmatrix} E_x e^{i\phi_x} \\ E_y e^{i\phi_y} \\ 0 \end{bmatrix} e^{i(\beta z - \omega t)}. \tag{4.1}$$

The Jones vector of the input state of polarization is:

$$\mathbf{J} = \begin{bmatrix} E_x e^{i\phi_x} \\ E_y e^{i\phi_y} \end{bmatrix}. \tag{4.2}$$

Thus, the Jones vector represents the amplitude and phase of the electric field in the x and y directions. By varying these parameters, using various photonic devices, the polarization of light can be changed.

Some of these polarization states have already been mentioned in the context of QKD and can be seen in the table 4.1.

Polarization	Jones vector	Ket notation
Linear polarized in the x direction	$\begin{bmatrix} 1 \\ 0 \end{bmatrix}$	$\|H>$
Linear polarized in the y direction	$\begin{bmatrix} 0 \\ 1 \end{bmatrix}$	$\|V>$
Linear polarized at 45° from the x axis	$\frac{1}{\sqrt{2}} \begin{bmatrix} 1 \\ 1 \end{bmatrix}$	$\|D>$
Linear polarized at -45° from the x axis	$\frac{1}{\sqrt{2}} \begin{bmatrix} 1 \\ -1 \end{bmatrix}$	$\|A>$
Right-hand circular polarized	$\frac{1}{\sqrt{2}} \begin{bmatrix} 1 \\ -i \end{bmatrix}$	$\|R>$
Left-hand circular polarized	$\frac{1}{\sqrt{2}} \begin{bmatrix} 1 \\ i \end{bmatrix}$	$\|L>$

Table 4.1: 6 common examples of normalized Jones vectors.

4.2 Development of integrated optical components

Waveguide

A waveguide is the fundamental element of integrated optics. It is used to guide electromagnetic waves through a device as electric wires are used to carry electric currents. Typical optical waveguides include the common optical fibers and other transparent dielectric waveguides made of plastic and glass. In most cases, light is confined in the core by total internal reflection. This occurs only if the dielectric index of the core, n_1, is higher than that of the surrounding layers, the cladding, n_2.

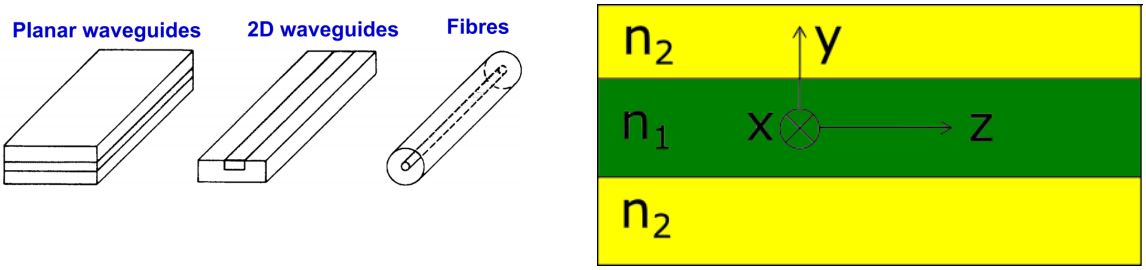

Figure 4.1: Left side: Common types of waveguides [86]. Right side: Schematic representation of a slab waveguide.

The equations that govern the behaviour of light inside these waveguides are obtained by applying Maxwell's equations to the system. Using a wave optics approach, light can be described by a sinusoidal time-varying wave propagating in the z direction. The propagation constant in the z direction is β. The electric and magnetic components of the wave are expressed as:

$$\begin{aligned} \vec{E} &= \vec{E_0}(x,y)e^{i(\beta z-\omega t)} \\ \vec{H} &= \vec{H_0}(x,y)e^{i(\beta z-\omega t)} \end{aligned}. \tag{4.3}$$

In the case of a slab waveguide (figure 4.1), some assumptions can be made to simplify the analysis.

First, no component of the fields varies in the x direction ($\frac{\partial}{\partial x} = 0$). The infinity of the x dimension of the layer in the slab allows this assumption.

Second, there is no electric field component in the z direction (TE modes). The field is composed of both TM and TE modes in general. For now, only the TE modes will be considered.

With these assumptions, Maxwell's equations lead to:

$$\nabla^2\vec{E} = \frac{\partial^2\vec{E}}{\partial x^2} + \frac{\partial^2\vec{E}}{\partial y^2} + \frac{\partial^2\vec{E}}{\partial z^2} = \frac{\partial^2\vec{E}}{\partial y^2} + \frac{\partial^2\vec{E}}{\partial z^2} = \frac{n_{1,2}^2}{c^2}\frac{\partial^2\vec{E}}{\partial t^2}, \tag{4.4}$$

$$\frac{\partial^2 E_x}{\partial y^2} + (n_{1,2}^2 k_0^2 - \beta^2)E_x = 0, \tag{4.5}$$

where $n_{1,2}^2$ is the refractive index in the core (n_1) and in the cladding (n_2), c is the speed of light and k_0 is the free-space wavenumber ($k_0 = \omega/c$).

There are two kinds of solutions for the differential equation 4.5. For positive values of $k_{y_{1,2}}^2 =$

$n_{1,2}^2 k_0^2 - \beta^2$, the solution takes the form of trigonometric solutions. For negative values, it takes the form of exponential solutions.

Choosing the solutions that fit the physical conditions of the guided wave, it is found that inside the core layer the wave is oscillatory and the trigonometric solutions are suitable. However, inside the cladding layer, only the evanescent wave is allowed and the solution must have a decaying nature. Thus, inside the core one has,

$$n_1^2 k_0^2 - \beta^2 = k_{y_1}^2 > 0 \quad => \quad E_x = A\cos(k_{y_1} y) + B\sin(k_{y_1} y), \tag{4.6}$$

and outside,

$$n_2^2 k_0^2 - \beta^2 = k_{y_2}^2 < 0 \qquad => \qquad E_x = Ce^{-k_{y_2} y} + De^{k_{y_2} y}, \tag{4.7}$$

where the factor $e^{i\omega t}$ was suppressed.

From these equations, the range of β is set to:

$$n_1 k_0 > \beta > n_2 k_0. \tag{4.8}$$

Although the waveguide is not a homogeneous medium, an effective refractive index can be defined, n_{eff}. This parameter can be calculated from $\beta = k_0 n_{eff}$. Thus, from equation 4.8, this value must be lower than the refractive index of the core and bigger than the cladding's.

From the boundary conditions, the constants A, B, C and D can be found. Then, the values of k_{y_1} and k_{y_2} must be determined as they are crucial to determining the modes of propagation.

Using the left part of equation 4.6 and equation 4.7,

$$(k_{y_1} d)^2 + (k_{y_2} d)^2 = V^2, \tag{4.9}$$

where $V = k_0 d\sqrt{n_1^2 - n_2^2}$. Since V comprises only physical constants such as the height of the guide d, the indices of refraction, and the light wavelength, V is referred to as the normalized thickness or normalized frequency of the guide. The normalized thickness V is an important parameter specifying the characteristics of the guide.

Using the right part of equation 4.6 and equation 4.7,

$$\left(\frac{n_2}{n_1}\right)^2 k_{y_1} d\tan k_{y_1} d = k_{y_2} d \qquad \text{and} \qquad -\left(\frac{n_2}{n_1}\right)^2 k_{y_1} d\cot k_{y_1} d = k_{y_2} d, \tag{4.10}$$

for even and odd solutions respectively.

From equations 4.9 and 4.10 graphical solutions to the values can be found. These solutions are called modes. The number of modes available depends on the value of V. The higher the value, the more modes the waveguide can support. This parameter can be controlled by adjusting the height of the slab for a material. If only a mode is supported, it is called a single mode waveguide. Otherwise it is called multi mode waveguide.

For each mode, a propagation value, β, is determined (from equation 4.6 or equation 4.7) and thus

the electric field is completely defined. The magnetic field can then be found using Maxwell equations.

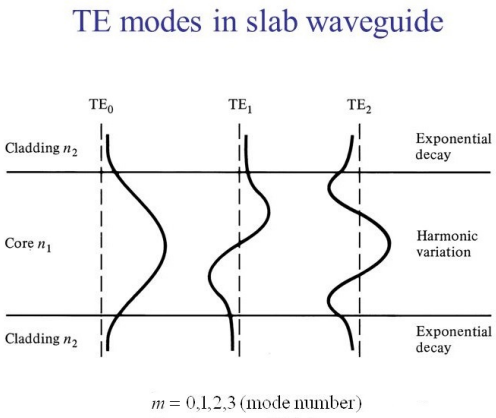

Figure 4.2: Schematic representation of the TE guided modes for a certain height of the slab. [87]

These solutions are for the transverse electric field. If a transverse magnetic field is assumed, similar modes are obtained.

This analysis was made for the simplest case, (slab waveguide) however, it gives an insight into the general physics at play. A waveguide can only support discrete guided modes for a given size. In this work, using waveguides fabricated by femtosecond laser direct writing, a single mode cylindrical waveguide is pursued.

For this case, the electric field takes the form, $E(r,\phi) = e^{-im\phi}E(r)$, where m is an integer that represents the number of times the phase rotates 2π. The complete derivation of the solution can be found in [88]. It takes the form of $E(r,\phi,z) = J_m(\sqrt{n^2k_0^2 - \beta_{nm}^2}r)e^{-im\phi}e^{-i\beta_{nm}z}$, where J_m is the Bessel function (1st kind) of order m. It can be seen that a discrete set of modes exist, given in this case by n, and m. Some of these solutions can be seen in figure 4.3.

This solution assumes that there is a small index contrast, so that the waveguide can be assumed to be only weakly guiding. The method studied in this work for constructing waveguides results in a slight difference between the refractive index of the core and the cladding, around $n_{core} - n_{cladding} = 10^{-3}$. These solutions are called the linearly polarized (LP) modes.

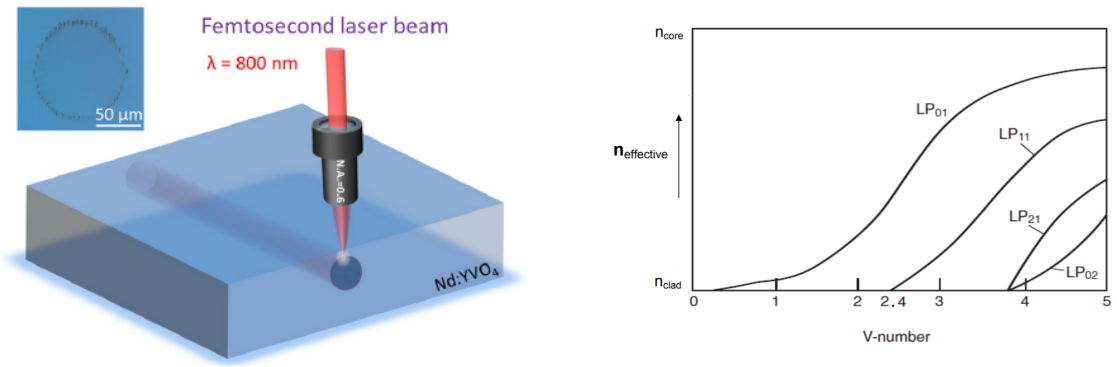

Figure 4.3: Left side: Example of a waveguide fabricated by femtosecond laser machining [89]. Right side: Dispersion curves for low order Linearly Polarized (LP) Modes of an Optical Fiber [90].

The lowest-order mode (LP_{01}) has an intensity profile which is similar to that of a Gaussian beam [91]. From [92], the fraction of power, η, in the core of radius a is given by:

$$\eta(a) = 1 - \frac{1}{V^2}, \tag{4.11}$$

for lowest-order mode of step index waveguides. This implies that to keep most of the power in the core, thus minimizing losses in cladding, the V value must be maximized.

Considering the normalized frequency parameter, $V = \frac{2\pi}{\lambda} a \sqrt{n_{core}^2 - n_{cladding}^2}$, one can estimate the number of modes allowed for a waveguide. For SM operation the V-parameter must be less than or equal to 2.405 (root of Bessel function), however realistically $V < 3$ is acceptable. In practice, one cannot really distinguish between the V value between 2.3 and 3.0. Experimentally observation shows that only one mode is still supported [92].

Optical energy can be lost from waveguided modes by radiation, in which case photons are emitted into the media surrounding the waveguide and are no longer guided. Radiation losses from either planar or straight channel waveguides are negligible for well-confined modes. For this reason, the losses in the straight waveguides are primarily due to fabrication and material imperfections and low compared to other photonic devices.

The transmission loss of highly purified glass has become as low as 0.15 dB/km at $\lambda = 1.55$ μm.

Nevertheless, waveguides fabricated by femtosecond laser direct writing have greater propagation losses due to the modes being not as well confined (lower difference between refractive indices of the bulk and core). Values below 0.5 dB/cm can still be expected.

These straight waveguides are the most basic building block for photonic circuits. They are commonly used to guide light performing no particular transformation and provide the lowest loss of any component. However, through interaction with other waveguides, complex devices may be created. For an ideal waveguide, without losses and with no birefringence, the Jones matrix is given by:

$$M_{wg} = e^{i\beta L} \begin{bmatrix} 1 & 0 \\ 0 & 1 \end{bmatrix}. \tag{4.12}$$

The output of a Jones vector after applying this matrix is just the electric field after propagating through a distance L of the waveguide. There is only a global phase factor, the same phase is applied to the electric field in the x and y directions. Therefore, the polarization is not changed.

Wave retarders

A wave retarder or waveplate is a fundamental component of optical systems. It changes the polarization of light while traveling through it. Two common types of waveplates are the half-wave plate, which shifts the polarization direction of linearly polarized light, and the quarter-wave plate, which converts linearly polarized light into circularly polarized light and vice versa.

A waveplate works by shifting the phase between two perpendicular polarization components of the light wave. A typical bulk optics waveplate is simply a birefringent crystal with a carefully chosen

orientation and thickness. The crystal has an optic axis that is commonly chosen to be parallel to the surfaces of the plate during the fabrication process. This results in two axes in the cut's plane: the fast axis, with a smaller refractive index and the slow axis, with a larger refractive index. Then, as the two components of light along these axes accumulate phase at different rates, after a certain distance, the polarization will be different. This expression can be written as:

$$\Delta\phi = k_0 \Delta n d, \tag{4.13}$$

where $\Delta\phi$ is the total phase change, Δn is the material birefringence and d is the thickness of the crystal.

This manipulation of the light's polarization happens in every birefringent material. When working with free space propagation, this is not a major concern as air is practically not birefringent. Nevertheless, most optical fibers and waveguides are. This means that propagation along these paths will result in changes in polarization.

This can be advantageous because the waveguides studied can create wave retarders with no modification to its design. However, it can also be a problem since every waveguide in the circuit will act as parasitic waveplate, unwantedly changing the polarization.

To control how the waveguide affects the polarization, three parameters must be controlled. The waveguide birefringence, the optical axis that determines the fast and slow axis and the length of the waveguide.

The birefringence value results from the fabrication process and material used. When using FLDW, typical values of $\Delta n \approx 10^{-5}$ [93] are expected when trying to minimize this effect. When trying to maximize it, values of the order of 10^{-4} [73] are usually obtained (higher values have been showed with more complex designs). An analysis of the fabrication process and how it affects the birefringence has been made in a previous chapter.

The optical axis is also a result of fabrication methods. Most waveguides are created with the fast axis along the vertical direction and the slow axis along the horizontal direction. Using techniques previously described, this can be changed and an almost arbitrary set of axis can be chosen.

The length of the waveguide can then be adjusted in order to suppress this effect (short waveguides), or to perform a change in polarization.

The manipulation caused by the waveplates can be described using a matrix formalism.

$$\begin{bmatrix} E_x \\ E_y \end{bmatrix} \longrightarrow \begin{bmatrix} e^{ik_0 n_x d} E_x \\ e^{ik_0 n_y d} E_y \end{bmatrix} = \begin{bmatrix} e^{ik_0 n_x d} & 0 \\ 0 & e^{ik_0 n_y d} \end{bmatrix} \begin{bmatrix} E_x \\ E_y \end{bmatrix} = e^{ik_0 n_x d} \begin{bmatrix} 1 & 0 \\ 0 & e^{ik_0 \Delta n d} \end{bmatrix} \begin{bmatrix} E_x \\ E_y \end{bmatrix}. \tag{4.14}$$

Quarter wave plate:

$$e^{ik_0 \Delta n d} = i <=> k_0 \Delta n d = \frac{\pi}{2} <=> d = \frac{1}{4}\frac{\lambda}{\Delta n}. \tag{4.15}$$

$$\begin{bmatrix} E_x \\ E_y \end{bmatrix} \longrightarrow e^{ik_0 n_x d} \begin{bmatrix} 1 & 0 \\ 0 & i \end{bmatrix} \begin{bmatrix} E_x \\ E_y \end{bmatrix}. \tag{4.16}$$

Half wave plate:

$$e^{ik_0 \Delta n d} = -1 <=> k_0 \Delta n d = \pi <=> d = \frac{1}{2}\frac{\lambda}{\Delta n}. \tag{4.17}$$

$$\begin{bmatrix} E_x \\ E_y \end{bmatrix} \longrightarrow e^{ik_0 n_x d} \begin{bmatrix} 1 & 0 \\ 0 & -1 \end{bmatrix} \begin{bmatrix} E_x \\ E_y \end{bmatrix}. \tag{4.18}$$

From these equations, it can still be seen a global phase that does not change the polarization. But now, there are different diagonal values in the matrices. As these values are different, they will change each electric field differently, changing the overall polarization.

The loss of this device can be modeled in the same way as a simple waveguide. This means the major contribution to the loss will be the size of the waveguide. In order to minimize the losses, the size must be minimized. However, in order to implement certain operations, a minimum length is required.

As the typical lengths required to create a waveplate are orders of magnitude bigger than the writing resolution, the length's fabrication tolerance is high.

Curved waveguides

Bent waveguides are necessary in almost all photonic designs. They are important as input/output waveguides for different devices, for example, directional couplers.

Because of distortions of the optical field that occur when guided waves travel through a bend in a channel waveguide, radiation loss can be increased. In fact, the minimum allowable radius of curvature of a waveguide is limited by radiation losses rather than by fabrication tolerances.

There are several methods to analyse radiation losses in bent waveguides. One intuitive way is the velocity approach developed by Marcatili and Miller [94]. The tangential phase velocity of waves in a curved waveguide must be proportional to the distance from the center of curvature because otherwise the phase front would not be preserved.

For example, considering a mode propagating in a circular waveguide with radius R and propagation constant β_z. For a certain radius, bigger than R + X_r, the phase velocity would have to exceed the velocity of unguided light (in the confining medium, with index n_1), in order to preserve the phase front. Since $\frac{d\theta}{dt}$ must be the same for all waves along the phase front, two resultant equalities can be written:

$$(R + X_r)\frac{d\theta}{dt} = \frac{w}{\beta_0} \qquad and \qquad R\frac{d\theta}{dt} = \frac{w}{\beta_z}, \tag{4.19}$$

where β_0 is the propagation constant of unguided light outside the waveguide. Combining both equalities, X_r can be obtained,

$$X_r = \frac{\beta_z - \beta_0}{\beta_0} R. \tag{4.20}$$

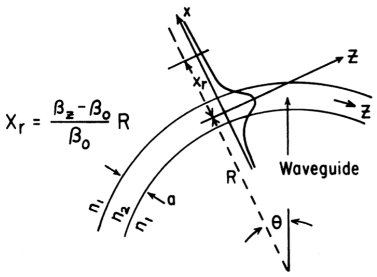

Figure 4.4: Diagram illustrating the velocity approach to the determination of radiation loss. [95]

.

The photons that cannot travel fast enough to keep with the mode are considered removed from the waveguide, radiated into the surrounding medium. This distance, Z_c, can be estimated by using the result from [96] where it has been shown that light emitted into a medium from an abruptly terminated waveguide remains collimated to within a waveguide thickness over a length Z_c given by:

$$Z_c = \frac{a^2}{2\lambda_1}, \tag{4.21}$$

where a and λ_1 are the near field beam width and the wavelength in the medium surrounding the waveguide.

The exponential attenuation coefficient is related to the power lost per unit length traveled in the guide by

$$\alpha = \frac{-1}{P(z)} \frac{dP(z)}{dz}, \tag{4.22}$$

where P(z) is the power transmitted.

If the power in the tail of the mode beyond X_r is defined as P_1 and the total power carried by the waveguide as P_t, the attenuation coefficient can expressed by

$$\alpha \approx \frac{1}{P_t} \frac{P_1}{Z_c}. \tag{4.23}$$

The distance Z_c can be conveniently determined from equation 4.21, but P_1 must be calculated by integration of the power contained in the optical mode for radius greater than R + X_r. While this calculation can be quite complex, it can be shown that the result takes the simple form of:

$$\alpha = C_1 e^{(-C_2 R)}, \tag{4.24}$$

where C_1 and C_2 are constants that depend on the dimensions of the waveguide, and on the shape of the optical mode.

The main result here is that the radiation loss in a curved waveguide decreases exponentially with the radius of the curve. This means that there is a radius for each waveguide for which the losses due to bending can be made negligible.

In fact, for a given design, a study of the parameters should be done in order to have a better estimation of losses in bent waveguides. A study made by [54] helps in establishing a magnitude for such radius using light near the optical spectrum. In this work, femtosecond laser direct writing is used to create curved waveguides for light with a wavelength of 1550 nm. The results for waveguides using 850 nm would be different because the waveguides characteristics would be different, however, the behaviour and magnitude would be close to the one seen here.

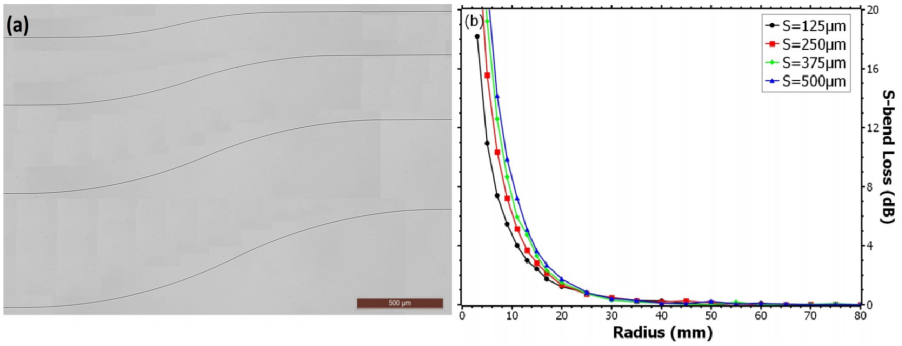

Figure 4.5: (a) Microscope images of s-bends (R=3 mm) with input and output waveguide separations of 125, 250, 375 and 500 μm from top to bottom respectively. (b) Bend loss in function of bend radius for different waveguide separations. [54]

According to [97], for practical values of bending radius, when $\frac{R}{a} > 10^3$ (the relation between the radius of curvature and the radius of the waveguide), the bending losses are negligible.

In [98], a directional coupler in borosilicate glass (EAGLE2000, Corning) was designed using (ULW) waveguides. At wavelengths around 800 nm, the waveguides supported a single Gaussian mode of circular profile with 8 μm diameter at $1/e^2$. Measured propagation losses were 0.5 dB/cm and using a curvature radius of 30 mm, additional bending losses were lower than 0.3 dB/cm. Straight segments and circular arcs of 30 mm radius were employed for an overall device length of 24 mm.

S-Bends

There are basically two kinds of S-bend waveguides: the S-bend waveguide consisting of a fixed radius of curvature R and the S-bend waveguide in which the radius of curvature varies continuously. In this work the latter case is used to create curved waveguides, specifically the version with the functional shape of a sinusoid.

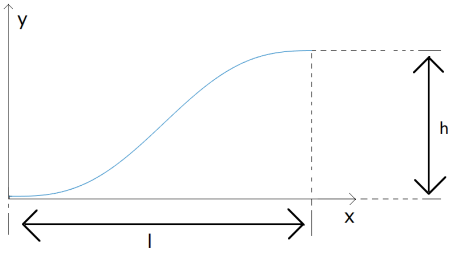

Figure 4.6: Schematic diagram of an S-shaped waveguide bend with a transition length l and a lateral offset h.

This shape can be expressed by:

$$y(x) = \frac{xh}{l} - \frac{l}{2\pi}\sin\left(\frac{2\pi x}{l}\right), \tag{4.25}$$

This particular form of transition has been found to be effective in achieving low loss, because it eliminates discontinuities in y, y' (the first derivative) and y" (the second derivative) of the function. An analysis of the loss is performed in [99]. Here, an expression for the total loss in this bent waveguide is derived.

$$\text{Loss}(dB) = \frac{10}{\ln(10)}\frac{C_1 l}{2\pi}e^{-\gamma}[3.5168 - 2.0843\log(\gamma)], \tag{4.26}$$

where $\gamma = \frac{C_2 l^2}{2\pi h}$, with the approximations used only valid for large values γ. This parameter is related to the radius of the curve and from the expression 4.26 it can be seen that for large values, the loss is negligible. This equation allows a better estimation of the S-bend parameters in order to minimize the loss.

From the point of view of the propagation of polarized light, the bent waveguides are not very different from the straight waveguides. The Jones matrix considered can be the same, meaning that the length of the curve is the most important parameter. For a planar curve in R^2 defined by the equation $y = f(x)$ and f being continuously differentiable, the arc length is then given by:

$$s = \int_{x_i}^{x_f} \sqrt{1 + \left(\frac{dy}{dx}\right)^2}\, dx, \tag{4.27}$$

where x_f and x_i are the final and initial x-coordinate of the curve. Applying this equation to the S-bend used, the length is:

$$s = \int_{x_i}^{x_f} \sqrt{1 + \left(\frac{h}{l} + \cos\left(\frac{2\pi x}{l}\right)\right)^2}\, dx. \tag{4.28}$$

This means the Jones matrix, if the birefringence is ignored is:

$$M_{cwg} = e^{i\beta s}\begin{bmatrix} 1 & 0 \\ 0 & 1 \end{bmatrix}. \tag{4.29}$$

As it can be seen, there is only a global phase, as with a simple waveguide. There is no change in polarization, as no birefringence was assumed. This assumption is reasonable if Type I waveguides are used and s is not high.

Directional coupler

Using curved waveguides, it becomes possible to develop new and more complex devices. For example, the directional coupler.

In bulk optics, two beams can be overlapped into one spatial mode using a beamsplitter. In integrated optics, this task can be fulfilled by a directional coupler, which architecture is depicted in Fig 4.7.

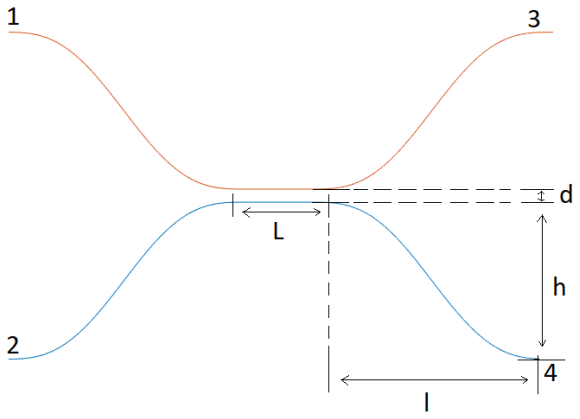

Figure 4.7: Design of a directional coupler with the control parameters represented.

Provided that both waveguides are separated by a small distance d within an interaction region of length L, the field of one guided beam can be transferred to another via evanescent coupling, allowing to overlap two beams launched in different waveguides into one output port. The splitting ratio depends directly on d and L, and the total length of the device is determined by the spatial separation of the ports and the achievable radius of curvature R. The radius results from the relation between l and h, with l>>h.

These devices can be approximately characterized by coupled mode theory for weakly coupled waveguides. This theory assumes that the modes in each waveguides remain approximately unchanged. The interaction between the modes only affects the amplitude of such modes and not their spatial profile and propagation constants.

Assuming that the unperturbed mode in a waveguide takes the form of $\vec{E_j}(x,y,z) = A_j(z)\vec{\varepsilon_j}(x,y)$, where A(z) is a complex amplitude which includes the phase term $e^{-i\beta z}$. The term $\vec{\varepsilon}$(x,y) is the solution for the field distribution of the mode in one waveguide, assuming that the other waveguide is absent. The coupling between modes is given by the general coupled mode equations for the amplitudes of the two modes. Thus,

$$\frac{dA_1}{dz} = i\beta_1 A_1 + k_{12}A_2, \qquad \frac{dA_2}{dz} = i\beta_2 A_2 + k_{21}A_1, \tag{4.30}$$

where β_1 and β_2 are the propagation constants of each waveguide and k_{12} and k_{21} are the coupling coefficients between waveguides. These coupling coefficients can be estimated by:

$$\begin{aligned} k_{12} &\approx \frac{1}{2}\left(n^2_{1_{\text{core}}} - n^2_{\text{cladding}}\right)\frac{k_0^2}{\beta}\int_{R^2}\vec{\varepsilon}_1(x,y)\vec{\varepsilon}_2(x,y)dxdy \\ k_{21} &\approx \frac{1}{2}\left(n^2_{2\ \text{core}} - n^2_{\text{cladding}}\right)\frac{k_0^2}{\beta}\int_{R^2}\vec{\varepsilon}_2(x,y)\vec{\varepsilon}_1(x,y)dxdy \end{aligned}. \tag{4.31}$$

Considering both waveguides to be identical, $\beta_1 = \beta_2 = \beta$ and $k_{12} = k_{21} = -iK$.

$$\begin{aligned} \frac{dA_1}{dz} &= -i\beta A_1 - iKA_2 \\ \frac{dA_2}{dz} &= -i\beta A_2 - iKA_1 \end{aligned}, \tag{4.32}$$

where,

$$\begin{aligned} C_{11} &= \cos(Kz) \qquad C_{12} = -i\sin(Kz) \\ C_{21} &= -i\sin(Kz) \qquad C_{22} = \cos(Kz) \end{aligned}, \tag{4.33}$$

with $K = \sqrt{k_{12}k_{21}}$

If it is assumed that light is coupled into guide 1 at the point z = 0, so that boundary conditions for the problem are given by:

$$A_1(0) = 1 \qquad \text{and} \qquad A_2(0) = 0, \tag{4.34}$$

then the solutions are described by:

$$\begin{aligned} A_1(z) &= \cos(Kz)e^{-i\beta z} \\ A_2(z) &= -i\sin(Kz)e^{-i\beta z} \end{aligned}. \tag{4.35}$$

This means that light coupled into port 1 will travel along the single mode waveguide and, as the waveguides get closer, light will be transferred to the other single-mode waveguide by evanescent coupling. If the waveguides are identical, coupling will continue until all power is in the opposite waveguide and past that distance, power will return to the original waveguide. This behavior is periodical and the interaction length defines the power splitting at the output ports 3 and 4.

This shows how this device can be used as an analogous beamsplitter. If the interaction length L is chosen carefully, half the power can exit through one output and the rest through the other. In this case, $Kz = \frac{\pi}{4}$ and therefore $L = \frac{\pi}{4K}$ would divide the power evenly.

If no birefringence is assumed, the directional coupler will act as a simple beamsplitter. Nevertheless, as previously discussed, these waveguides may have birefringence values that cannot be neglected.

The Jones Matrix of a directional coupler is harder to define as there are two beams. However, in this work, there will only ever be one input active at a given time and interest in only one output. This simplifies this problem. The directional coupler can be divided into two parts. The S-bend, with a corresponding Jones Matrix already defined, and that appears twice and the interacting waveguide. The Jones Matrix of this last part will be defined by the choice of output and input waveguide. From the solutions in equation 4.35, when the chosen output is the same waveguide as the input,

$$M_{intwg} = \cos(Kz)e^{-i\beta z}\begin{bmatrix} 1 & 0 \\ 0 & 1 \end{bmatrix}. \tag{4.36}$$

If they are opposite,

$$M_{intwg} = -i\sin(Kz)e^{-i\beta z}\begin{bmatrix}1 & 0\\ 0 & 1\end{bmatrix}. \tag{4.37}$$

The complete Jones Matrix of the direction coupler will then be:

$$M_{DC_1} = e^{i2\beta s}\cos(Kz)e^{-i\beta z}\begin{bmatrix}1 & 0\\ 0 & 1\end{bmatrix}. \tag{4.38}$$

Or,

$$M_{DC_2} = -e^{i2\beta s}i\sin(Kz)e^{-i\beta z}\begin{bmatrix}1 & 0\\ 0 & 1\end{bmatrix}. \tag{4.39}$$

With these equations it can be shown that this directional coupler can be used as a beam splitter, splitting the field from one waveguide to both. The size of the directional coupler will depend on the parameter K, responsible for this effect.

It can be seen that there is a global phase and an amplitude modulation term. Neither the global phase nor the amplitude term will affect the polarization as they affect both the x and y field in the same way. The new amplitude term will be responsible for the amount of light at each output.

Polarizing Directional coupler

Previously, the analysis of a directional coupler device was done without considering birefringence. Nevertheless, the coupling strength, K, depends on the refractive index of the waveguide which is polarization dependent due to the intrinsic birefringence. This means that the rate of light transferred between waveguides is different for H (horizontal) and V (vertical) polarization or other polarizations. As such, this is a polarizing device that may behave similar to polarizing beam splitter.

In reality, the coefficient K is better estimated by:

$$K_{H,V} \approx \frac{1}{2}(n^2_{core,H,V} - n^2_{cladding,H,V})\frac{k_0^2}{\beta}\int_{R^2}\vec{\varepsilon}_{1,H,V}(x,y)\vec{\varepsilon}_{2,H,V}(x,y)dxdy, \tag{4.40}$$

where, K_H and K_V are the coupling coefficients for the horizontal and vertical polarization and the waveguides are identical (K=k_{12}=k_{12}). Anisotropic guiding properties give rise to the difference between the coupling coefficients due to deviations in both the effective mode index and the spatial mode profile.

Considering K_V and K_H different due to this birefringence, the beat lengths of H and V modes differ, allowing to choose an optimal interaction length of the device corresponding to the distribution of orthogonally polarized states of light to distinct output modes of the coupler. This has been showed by different teams [73].

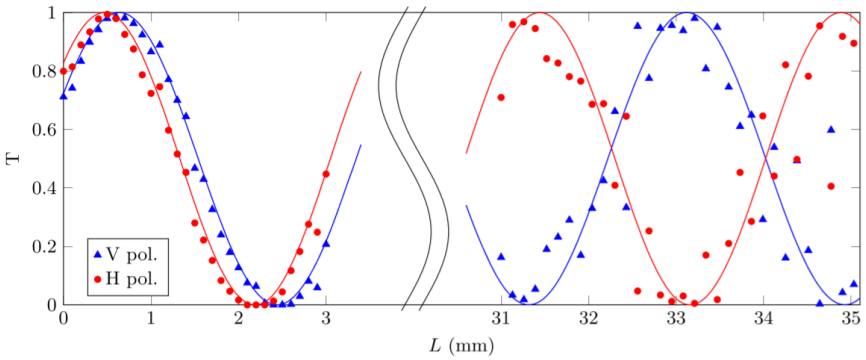

Figure 4.8: Experimental measurements of the transmission T of DCs with different interaction length L and waveguide separation d=12.5 μm, for H (red circles) and V (blue triangles) polarised input light. Solid lines are best-fitting theoretical curves. Error bars are smaller or comparable to the marker size.[73]

The main parameter that determines the length necessary to separate the different polarizations is coupling coefficient K. As it depends on the spatial profile of the electric field and the refractive indexes for each polarization, it can be quite hard to control. One way of doing this is by varying the distance between waveguides. As the coupling coefficient K depends on the overlap integral between the two waveguide modes, it depends on separation d between the two waveguides. For weakly guiding, femtosecond laser written waveguides, such dependency is well approximated by an exponential function of the kind:

$$K_{H,V} = K_{0(H,V)} e^{-\frac{d}{d_{0(H,V)}}}. \tag{4.41}$$

This equation only holds for a low range of values and thus only allows for fine tuning of the birefringence [100]. Other alternatives include using polarized light when writing the waveguides or stress inducing structures that increase the anisotropy.

These and other methods have been described and studied in a previous chapter.

These devices have some interesting functions. For example, and more important for this work, if the length is chosen to separate the orthogonal polarizations into different outputs, the polarizing beam splitter in the original design can be replaced. The device would have two inputs, but only one active at a given time. Only one output would be relevant for this work and the polarization of the light at that output would be dependant on which input was active. To sum up, this polarizing directional coupler would not only guarantee the spatial overlap of the light coming from two sources, but also, it would manipulate the output polarization of each input.

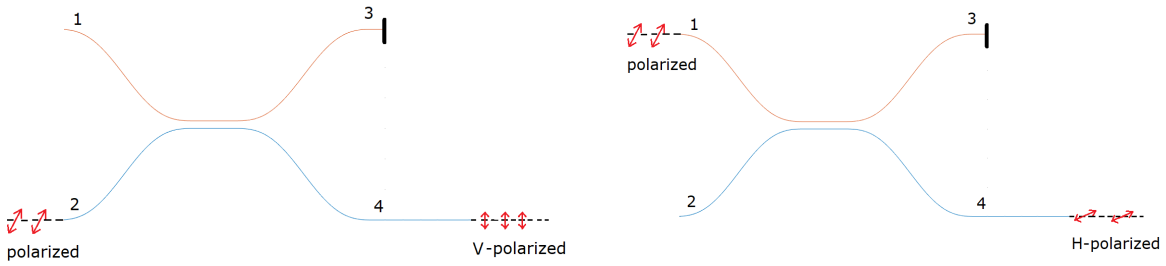

Figure 4.9: Example of how the polarizing beam coupler can be used to replace the polarizing beam splitter.

The Jones Matrix of this device will then be:

$$M_{DC_1} = e^{i2\beta s} e^{-i\beta z} \begin{bmatrix} \cos(K_H z) & 0 \\ 0 & \cos(K_V z) \end{bmatrix}. \tag{4.42}$$

Or,

$$M_{DC_2} = -e^{i2\beta s} i e^{-i\beta z} \begin{bmatrix} \sin(K_H z) & 0 \\ 0 & \sin(K_V z) \end{bmatrix}. \tag{4.43}$$

An important difference can be seen here. The amplitude terms previously observed outside the matrix are now inside and different for each electric field. This means that these fields will change in different ways and therefore, the polarization will be altered.

By experimentally finding the values of K_H and K_V, it is possible to obtain the necessary length for separating the polarizations.

This length will typically be much bigger than the lengths of previous devices because the difference between K_H and K_V is small.

One major disadvantage of this method is that it does not change the polarization, it separates its components. This means that if in the input, both components do not have the same intensity, the intensity of each state will be different. This is especially bad for the purpose of this work, as it makes it possible for Eve to extract information from the intensity of each photon. A possible solution is to polarize the light at the input in a way that it splits evenly or by attenuating one output more done the other.

In addition, this component assumes that the light at the inputs is polarized in the same way.

4.3 Integrated photonic design for QKD

As explained before, using waveguides and the birefringent properties of materials, the polarization of light can be controlled while guiding it through waveguides. From figure 2.4, it can be seen that the essential optical elements needed to perform the BB84 protocol are mirrors, beam splitters, half-wave plates and polarizing beam splitters.

Equivalent elements in integrated optics have been design. Therefore, starting from the design using bulk optics, a similar design can be obtained with integrated optics.

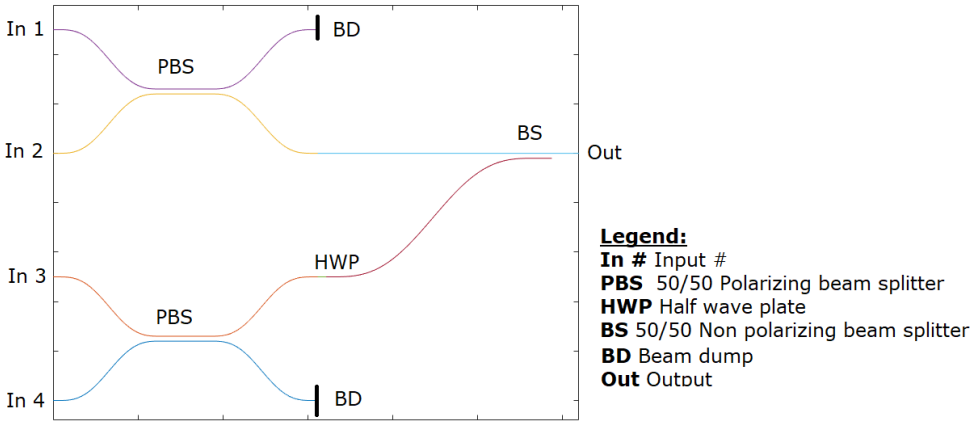

Figure 4.10: Schematic design of a possible integrated photonic circuit to reproduce the BB84 protocol.

The design in figure 4.10, while just a scheme, illustrates how to reproduce figure 2.4 with the elements designed previously. There are still four inputs numbered from 1 to 4. The first input is followed by a polarizing directional coupler design intending to be a polarizing beam splitter. The light linearly polarized at this input will come out horizontally polarized at the output, while from input 2, a vertically polarized state will come out. For this, the interaction length has to be carefully chosen as discussed before.

These two inputs are distanced from the other two in other not to interact. Input 3 and 4 go through an identical directional coupler and the same output follows. On this side, a half-wave plate, created by a waveguide with a higher birefringence, rotates the polarization in order to create the diagonally and anti-diagonally polarized states.

Then, the two outputs are combined in the same output waveguide using a non-polarizing directional coupler. This way, each input corresponds to a different optical path and therefore, a different final state or polarization.

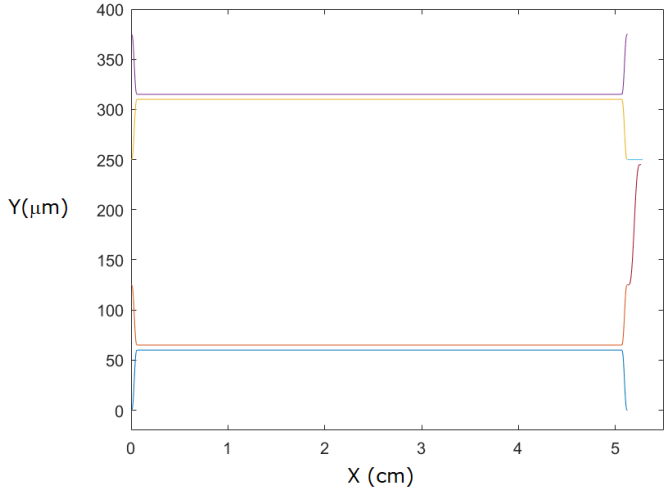

Figure 4.11: Same design as in figure 4.10 with the correct size and scale.

Figure 4.11 shows the integrated circuit in scale. On the y-axis, a distance of 125 μm was chosen because a VCSEL array with this distance between emitters was acquired as a potential replacement for the diode lasers. The size on x-axis was determined by the length of the photonic elements. Most of the length of the device comes from the polarizing directional coupler. As studied before, due to the usual values of birefringence obtained, a significant size is required to reproduce the expected results.

Material (Glass)	Pulse width (fs)	Wavelength (nm)	Rep. Rate (kHz)	Prop. Loss (dB/cm)	Ref.
Bismuth Borate	150	800	250	0.21 ± 0.14	[67]
Fused Silica	300	1044	500	0.5±0.1	[68]
Fused Silica	150	800	100	0.3 ± 0.1	[69]
Borosilicate	400	1040	960	0.2 ± 0.1	[72]
Borosilicate	300	1030	1000	0.3 ± 0.1	[73]
FOTURAN^{TM}	150	775	1	0.5 ± 0.1	[101]

Table 4.2: Propagation loss of some FLDW waveguides and the laser parameters used.

Using an average value for the birefringence, the length of the polarizing directional coupler is around 5 cm. As stated before, an estimated loss of 0.5 dB/cm is to be expected and it can be seen that this value is higher than all from the table 4.2. As the curves are not a significant source of the size of the device, the radius can be adjusted to minimize the bend loss, making the additional bending losses as small as desired or possible. From the figure 4.5 and assuming a bending radius of 40 mm, the curves would give additional bending losses of 0.4 dB. The coupling losses are closely related to the mode profile of the waveguide. With a careful choice of parameters and methodology, this mode profile can be made to match that of the optical fiber used, minimizing coupling losses. If a coupling loss of 1 dB is assumed, it is still higher than those from the articles in 4.2. Finally, it is assumed that the discontinuities due to different values of birefringence causes only 0.3 dB of additional losses, as evaluated in [72].

With all these assumptions, a general estimate for the overall loss would be around 4.3 dB.

In [72], the whole chip for tomography yields losses of 4.4 dB (including coupling losses, propagation and bending losses). The values are close to each other.

While this result is only an estimation taking into consideration different values in the literature, it allows to access the theoretical validity of the design. Here, a total length of 5.2 cm for the photonic circuit with a loss of 4.3 dB would result in a functional design and with a typical value for the overall loss. The size and weight (negligible) would allow for small-scale applications like a nano-satellite. Furthermore, this approach is more flexible. A 3D implementation is possible using the same design, as can be seen in figure 4.12.

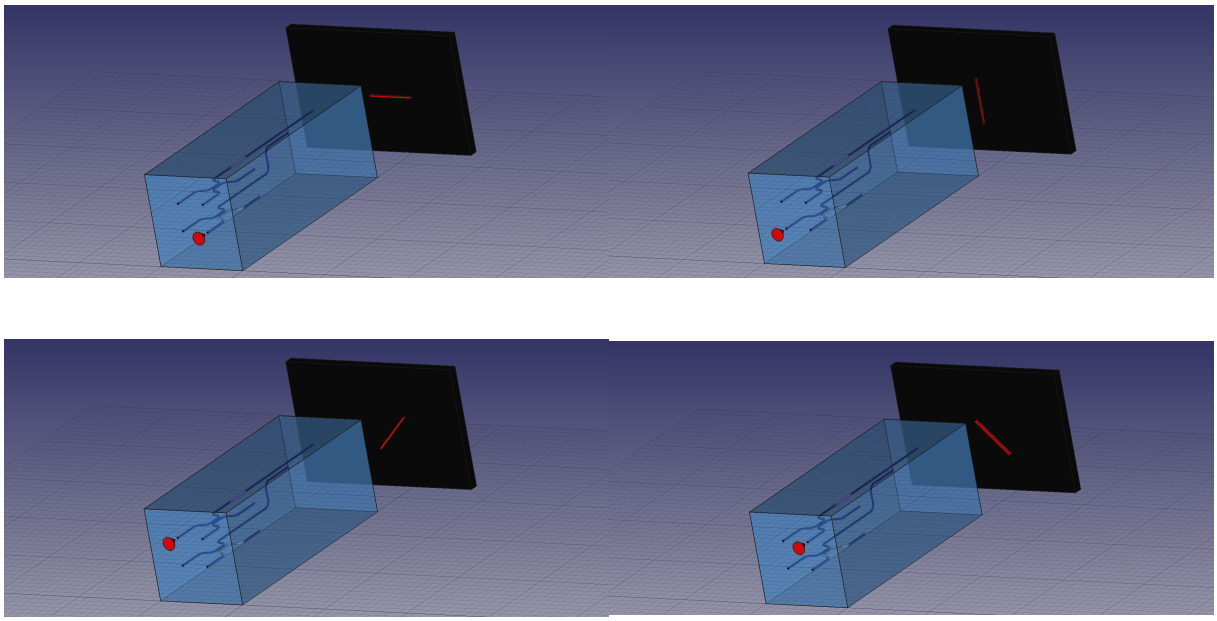

Figure 4.12: 3D schematic implementation of the design studied. The different images show the output polarization (a red line) as a function of which input is on. Upper Left: Horizontal polarization. Upper Right: Vertical polarization. Lower Left: Diagonal polarization. Lower Right: Anti-Diagonal polarization.

This approach was considered, but for now it will not be pursued. The rest of the equipment is made for a planar design, and a 3D design would not bring an overall advantage. Nevertheless, with this fabrication method it is possible and there can be situations in which it would prove advantageous.

4.4 Chapter overview and discussion

In this chapter, various passive components were explored. It was shown how they can be created from simpler components, how they affect the polarization, how they can replicate bulk optics elements and how to estimate the loss. With the analysis made here, it is possible to design circuits that can perform

different goals and recreate bulk optics experiments in an integrated photonic chip. Furthermore, an estimation of the loss on such devices is possible as well as an understanding of its limitations.

Then, the integrated photonic design was proposed. It comes from the bulk optics approach, but using the integrated components studied. This design was compared in term of losses to other works and shown to be functional on that front. Furthermore, a 3D alternative was shown but not explored. In the future, a prototype should be made in other to access limitations and possible changes to the design.

While not explored in this work, an interesting topic to study would be how ring resonators can be fabricated and integrated into current designs. These elements are already commonplace in integrated optics, but not as a polarization component. With a birefringent ring resonator that allowed light to loop N number of times, the size of an element could be reduced. This could prove useful for several components.

Chapter 5

Towards an efficient photon pairs source

Until now, the source of single photons used was always based on weak coherent pulses. However, due to the acquisition of a PPKTP crystal, an alternative source can be made and different protocols explored. The reason for this is that PPKTP crystals can create spontaneous parametric down-conversion.

Spontaneous parametric down-conversion (SPDC) was first observed in 1967 [102] and is a common technique in quantum optics, both as a source of entangled photon pairs and heralded single photons. SPDC is a non-linear optical process where a photon spontaneously splits into two other photons of lower energies, conserving both energy and momentum. These two conditions are central for the mechanism to happen and can be expressed in two simple equations, the phase-matching conditions.

$$\hbar\omega_1 = \hbar\omega_2 + \hbar\omega_3. \tag{5.1}$$

$$\mathbf{k_1} = \mathbf{k_2} + \mathbf{k_3}. \tag{5.2}$$

The most energetic photon is called the pump photon, while the resulting ones are called the signal and idler (for historical reasons). From now on, the indices p,s,i will be used rather than 1,2,3 when talking about the three-wave mixing phenomenon SPDC.

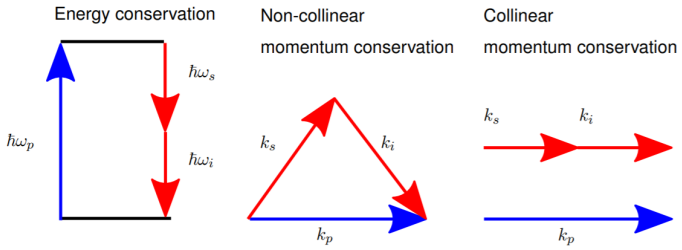

Figure 5.1: The phase matching conditions. Left: The energy of the pump is equal to the sum of the energy of the signal and idler. Center: When angle phase matched, the pump and down converted modes are usually non-collinear. The wave vectors obey momentum conservation. Right: When pumped in a collinear geometry momentum is still conserved. [103]

5.1 Analysis of spontaneous parametric down-conversion

In order to understand the theory behind this process, a quantum optics approach is necessary. Quantum optics deals with individual photons, quantified energy and momentum of the electromagnetic field, instead of only considering the wave-like properties of light. For a complete derivation and understanding of the quantization of the electromagnetic field, other resources are recommended [104].

Using Maxwell's equations for arbitrary dielectrics, the rate of change of the energy of the electromagnetic field U_{EM} can be expressed purely in terms of fields as:

$$\frac{dU_{EM}}{dt} = \int d^3r \left(\mathbf{H} \cdot \frac{d\mathbf{B}}{dt} + \mathbf{E} \cdot \frac{d\mathbf{D}}{dt} \right), \tag{5.3}$$

where $\mathbf{D} = \epsilon_0 \mathbf{E} + \mathbf{P}$, and $\mu_0 \mathbf{H} = \mathbf{B} - \mu_0 \mathbf{M}$.

Assuming the material non-magnetic ($\mu_0 \mathbf{H} = \mathbf{B}$) and the frequency spectrum of the light is off-resonance with the material's electrons, the material is approximately lossless. Finally, as the pump's light is weak compared to the electric field binding electrons to their atoms, the polarization field $\mathbf{P}$ is expressible as a rapidly decaying power series in $\mathbf{E}$:

$$P_a = \epsilon_0 \left[\chi^{(1)}_{ab} E_b + \chi^{(2)}_{abc} E_b E_c + \chi^{(3)}_{abcd} E_b E_c E_d + \ldots \right]. \tag{5.4}$$

The Einstein summation convention is used to simplify notation. $\chi^{(1)}$ and $\chi^{(2)}$ are the first- and second-order optical susceptibility tensors. Therefore, the general form of $\chi^{(2)}_{abc}$ for a given set of three fields is a 3x3x3 tensor, however, the permutation symmetry of the elements along with symmetry properties of uniaxial crystals can be invoked to reduce this number significantly.

In this regime, with just the first and second order contributions, the total energy rate simplifies to:

$$\begin{aligned} \frac{dU_{EM}}{dt} =& \frac{1}{2} \int d^3r \frac{d}{dt} \left(\mathbf{H} \cdot \mathbf{B} + \mathbf{D} \cdot \mathbf{E}^{(1)} \right) \\ &+ \frac{1}{3} \epsilon_0 \int d^3r \frac{d}{dt} \left(\chi^{(2)}_{psi} E_p E_s E_i \right). \end{aligned} \tag{5.5}$$

Here, $\mathbf{E}^{(1)}$ is the electric field up to first order.

The Hamiltonian of the electromagnetic field is now expressible as a sum of two terms, one governing the linear optical response, and one governing the nonlinear response, $H_{EM} = H_L + H_{NL}$.

The pump mode is aligned with the z-axis and treated as a classical monochromatic field of amplitude E^0_p (assuming the pump is sufficiently narrowband). It is further assumed that there is no significant depletion of the pump in the down conversion crystal. The electrical field of the pump can thus be written as:

$$\mathbf{E}_p(\mathbf{r}, t) = \frac{1}{2} \left[\mathbf{E}^{(+)}_p(\mathbf{r}, t) + \mathbf{E}^{(-)}_p(\mathbf{r}, t) \right] = \frac{1}{2} \left[E^0_p \mathbf{e}_p g_p(\mathbf{r}) e^{-i\omega_p t} + \text{ H.c. } \right], \tag{5.6}$$

with a polarization vector $\mathbf{e}_p$, a corresponding angular frequency ω_p and spatial distribution $g_p(\mathbf{r})$. The term H.c. means the Hermitian conjugate.

As the beam propagates through the z-axis, assuming the pump field to be sufficiently well-collimated,

to a good approximation, the longitudinal dependence of the pump field can be factored out.

At this point, the transverse momenta $\mathbf{q_p}$, $\mathbf{q_s}$, and $\mathbf{q_i}$ are defined as the projections of the pump wave vector $\mathbf{k_p}$, the signal wave vector $\mathbf{k_s}$, and the idler wave vector $\mathbf{k_i}$, onto the plane transverse to the optic axis, respectively. The components k_{pz}, k_{sz}, and k_{iz} are also defined as the longitudinal components of the corresponding wave vectors. This means the spatial profile of the beam can be written as:

$$g(\mathbf{r}) = \int d^2 q_p G(\mathbf{q_p}) e^{-i\mathbf{q_p}\cdot\mathbf{r}} e^{-ik_{pz}z}, \tag{5.7}$$

where $G(\mathbf{q_p})$ is the transverse field distribution in momentum space which propagates along the z-axis of the crystal with transverse momentum $\mathbf{q_p}$.

As for the signal and idler fields, they are quantized as field operators.

In a medium of index of refraction n, the electric displacement scalar operator $\hat{E}_j(\mathbf{q}, t, z)$ is expressible as a sum over momentum modes in a rectangular cavity of volume V, with polarization j. For convenience, $\hat{E}_j(\mathbf{q}, t, z)$, is separated into positive and negative frequency components $\hat{E}_j^+(\mathbf{q}, t, z)$, $\hat{E}_j^-(\mathbf{q}, t, z)$, where,

$$\hat{E}_j^{(+)} = \sum_{\mathbf{k}} E_{j\mathbf{k}} \hat{a}_{j\mathbf{k}} e^{i(\mathbf{q}\cdot\mathbf{r} - \omega_{j\mathbf{k}} t)} e^{ik_z z}, \tag{5.8}$$

in which, $\hat{a}_{j\mathbf{q}}$ is the annihilation operator for the mode with polarization j and wave number $\mathbf{k} = \mathbf{q} + k_z \mathbf{e_z}$. The dispersion relation inside the crystal is $|\mathbf{k}| = \omega_{j\mathbf{k}} n_{j\mathbf{k}}/c$, with $n_{j\mathbf{k}}$ the index of refraction and

$$E_{j\mathbf{k}} = i \left(\frac{\hbar \omega_{j\mathbf{k}}}{2\varepsilon_0 n_{j\mathbf{k}}^2 V} \right)^{1/2}. \tag{5.9}$$

The creation and annihilation operators are normalized so that:

$$\left[\hat{a}_{j\mathbf{q}}, \hat{a}_{m\mathbf{l}}^\dagger \right] = \delta_{jm} \delta_{\mathbf{ql}}. \tag{5.10}$$

Using the derivation of conjugate canonical variables just like in the case of a quantized harmonic oscillator, $\hat{a}$ being the photon annihilation operator (accounting for the disappearance of a photon) and $\hat{a}^\dagger$ the photon creation operator (accounting for the appearance of a photon), the quantum Hamiltonian describing linear-optical effects becomes:

$$\hat{H}_L = \sum_{\mathbf{k}} \hbar \omega_{\mathbf{k}} \left(\hat{N}_{j\mathbf{k}} + \frac{1}{2} \right) = \sum_{\mathbf{k}} \hbar \omega_{j\mathbf{k}} \left(\hat{a}_{j\mathbf{k}}^\dagger \hat{a}_{j\mathbf{k}} + \frac{1}{2} \right). \tag{5.11}$$

Where $\hat{N}_{j\mathbf{k}}$ is the photon number operator giving rise to the number $N_{j\mathbf{k}}$ photons in the electromagnetic mode $\mathbf{k}$ with polarization j and the following relations holds:

$$\begin{aligned} \hat{a}_{\mathbf{k}}^\dagger |vac\rangle &= |1_{\mathbf{k}}\rangle, \\ \hat{a}_{\mathbf{k}} |1_{\mathbf{k}}\rangle &= |vac\rangle. \end{aligned} \tag{5.12}$$

This means a single photon in mode $\mathbf{k}$ is created from the vacuum state $|vac\rangle$ and a single photon in mode $\mathbf{k}$ "disappears", for instance, because of absorption from a single dipole.

As one can see, the linear Hamiltonian cannot be responsible for the creation of photon pairs, as it is only first order in both the creation and annihilation operators.

Depending on which nonlinear coefficient mediates the interaction, one distinguishes between type-0 (pump, signal, and idler co-polarized), type-I (signal and idler co-polarized, but orthogonal to pump), or type-II (signal and idler polarizations orthogonal) SPDC. In this work, the type-II collinear case is addressed. Then the modes may be labeled by the angular frequency and the polarization where, $k_s(\omega) = \omega n_s(\omega)/c$ and $k_i(\omega) = \omega n_i(\omega)/c$.

The nonlinear quantum Hamiltonian, $\widehat{H}_{NL}$ can be written as:

$$\widehat{H}_{NL} = \epsilon_0 \frac{1}{3} \int d^3r \chi^{(2)}_{jkl} \mathbf{E}_p \hat{\mathbf{E}}_s \hat{\mathbf{E}}_i, \tag{5.13}$$

is a sum over eight distinct terms. Various combinations of these terms correspond to different basic nonlinear-optical processes, but only those processes that conserve energy contribute significantly to the probability-amplitude of down-conversion. For example, the two terms that are third-order in either photon creation or annihilation may be excluded, as their contribution to the probability amplitude of photon pair generation is negligible. Furthermore, for many nonlinear media, $\chi^{(\mathbf{2})}$ is only significant for one particular optical process (can be engineered by design).

When the nonlinear material has only a single relevant non-zero tensor coefficient, the susceptibility tensor contracted with the unit vectors of the field operators reduces to a scalar effective nonlinear coefficient $\left(\text{for example, } \chi^{(2)}\mathbf{e_x e_x e_y} = \chi^{(2)}\mathbf{e_p e_s e_i} = \chi^{(2)}_{eff}\right)$.

In the case of SPDC, either pump photons are destroyed in exchange for signal-idler photon pairs or vice versa, so that $\widehat{H}_{NL}$ is well-approximated as:

$$\hat{H}_{NL} \sim \hat{H}_{SPDC} = \frac{1}{3}\epsilon_0 \chi^{(2)}_{eff} \int_{-\infty}^{\infty} dxdy \int_{-L_z/2}^{L_z/2} dz E_p^{(+)} \hat{E}_s^{(-)} \hat{E}_i^{(-)} + \text{(H.c.)}. \tag{5.14}$$

From here, using the definitions and assumptions done before, the Hamiltonian becomes:

$$\begin{aligned}
\hat{H}_{SPDC} =& \frac{6}{3}\epsilon_0 \chi^{(2)}_{eff} \int dV \int d^2q_p \frac{E_p^0}{2} G(\mathbf{q_p}) e^{i\mathbf{q_p}\cdot\mathbf{r}} e^{ik_{pz}z} e^{-i\omega_p t} \\
&\times -i \sum_{\mathbf{k_s}} \sqrt{\frac{\hbar\omega_s}{2\epsilon_0 n_s^2 V}} e^{-i\mathbf{q_s}\cdot\mathbf{r}} e^{-ik_{sz}z} e^{i\omega_s t} \hat{a}^\dagger_{\mathbf{k_s},\omega_s} \\
&\times -i \sum_{\mathbf{k_i}} \sqrt{\frac{\hbar\omega_i}{2\epsilon_0 n_i^2 V}} e^{-i\mathbf{q_i}\cdot\mathbf{r}} e^{-ik_{iz}z} e^{i\omega_i t} \hat{a}^\dagger_{\mathbf{k_i},\omega_i} \\
&+ \text{ H.c.}).
\end{aligned} \tag{5.15}$$

$$\hat{H}_{SPDC} = -\frac{\sigma}{V}\phi(\omega_s,\omega_i) \sum_{\mathbf{k_s},\mathbf{k_i}} \Phi(\Delta\mathbf{k}) e^{-i\Delta\omega t} \hat{a}^\dagger_{\mathbf{k_s},\omega_s} \hat{a}^\dagger_{\mathbf{k_i},\omega_i} + \text{H.c.}, \tag{5.16}$$

$$\sigma = \chi^{(2)}_{eff} \hbar E_p^0, \tag{5.17}$$

$$\phi(\omega_s,\omega_i) = \frac{\sqrt{\omega_i\omega_s}}{n_s n_i}, \tag{5.18}$$

$$\begin{aligned}\Phi(\Delta\mathbf{k}) &= \int_{-\infty}^{\infty} dxdy \int d^2q_p G(\mathbf{q_p}) e^{-i\Delta q_x x} e^{-i\Delta q_y y} \int_{-L/2}^{L/2} dz e^{-i\Delta k_z z} \\ &= L \int d^2q_p G(\mathbf{q_p}) \delta(\Delta q_x)\delta(\Delta q_y) \text{sinc}\left(\frac{\Delta k_z L}{2}\right) \\ &= LG(\mathbf{q_s}+\mathbf{q_i}) \text{sinc}\left(\frac{\Delta k_z L}{2}\right).\end{aligned} \tag{5.19}$$

As in most experimental setups, the nonlinear crystal is a simple rectangular prism, centered at $\mathbf{r} = 0$, and with side lengths L_x, L_y, and L_z. Here, for now, it is assumed that the crystal is isotropic, so that $\chi^{(2)}$ does not depend on $\mathbf{r}$ and of infinite transverse x, y extent, which is justified when the beam diameter is much smaller than the crystal dimensions. A frequency mismatch $\Delta\omega = \omega_p - \omega_s - \omega_i$, a transverse wavenumber mismatch $\Delta\mathbf{q} = \mathbf{q_p} - \mathbf{q_s} - \mathbf{q_i}$ and a wavenumber mismatch $\Delta k_z = k_{pz} - k_{sz} - k_{iz}$ were introduced for convenience.

$$\lim_{V\to\infty} \frac{1}{V} \sum_{\mathbf{k_s}} = \frac{1}{(2\pi)^3} \int d^3\mathbf{k_s}. \tag{5.20}$$

With the Hamiltonian defined, it is possible to find the state of the system. In the interaction picture, given the starting state $|\Psi_{\text{initial}}\rangle$ at t_1, the state at a time t_2, after the interaction is complete, is then:

$$|\Psi_{\text{final}}\rangle = \exp\left(-\frac{i}{\hbar}\int_{t_1}^{t_2} dt \hat{H}_{SPDC}\right)|\Psi_{\text{initial}}\rangle, \tag{5.21}$$

where,

$$|\Psi_{\text{initial}}\rangle = |\mathbf{k_p}, \omega_p\rangle_p \otimes |\text{vac}\rangle_s |\text{vac}\rangle_i. \tag{5.22}$$

Then, given that the interaction strength is small, this exponential can be expanded and anything beyond the second term discarded. This is equivalent to stating that the probability of generating one pair of photons within each interaction period is small and the probability of generating two is negligible.

$$|\Psi_{\text{final}}\rangle_{s,i} = \{|\text{vac}\rangle_s|\text{vac}\rangle_i - \underbrace{\frac{i}{\hbar}\int_{t_1}^{t_2} dt \hat{H}'_{SPDC}|\text{vac}\rangle_s|\text{vac}\rangle_i\}}_{|\Psi\rangle^{(2)}_{s,i}} + O(2). \tag{5.23}$$

Since we are interested in the SPDC once a steady-state condition has been reached, the integration limits can also be extended to infinity ($t_1 \to -\infty$ and $t_2 \to \infty$). The resulting delta function can be interpreted as the energy conservation condition:

$$\begin{aligned}|\Psi\rangle^{(2)}_{s,i} &= \sigma\phi(\omega_s,\omega_i)\frac{1}{(2\pi)^6}\int\int d\mathbf{k_s}d\mathbf{k_i}\Phi(\Delta\mathbf{k})\int_{-\infty}^{\infty} dt e^{-i\Delta\omega t}\hat{a}^\dagger_{\mathbf{k_s}}\hat{a}^\dagger_{\mathbf{k_i}}|\text{vac}\rangle|\text{vac}\rangle \\ &\propto L\sigma \underbrace{\phi\Big(\omega_s,\omega_p-\omega_s\Big)}_{\text{Spectral distribution}}\int\int d\mathbf{k_s}d\mathbf{k_i}\underbrace{\text{sinc}\left(\frac{\Delta k_z L}{2}\right)}_{\text{Phase matching}}\underbrace{G\Big(\mathbf{q}_s+\mathbf{q}_i\Big)}_{\text{Spatial distribution}}|\omega_s,\mathbf{k_s}\rangle|\omega_p-\omega_s,\mathbf{k_i}\rangle.\end{aligned} \tag{5.24}$$

Note that the Hermitian conjugate portion of the Hamiltonian is gone, as it contains lowering operators

acting on the vacuum. It can be observed that this result shows that the signal and photons are only produced in pairs.

Phase matching

From equation 5.24, it can be seen that the amplitude of the SPDC process depends on sinc $\left(\frac{\Delta k_z L}{2}\right)$.

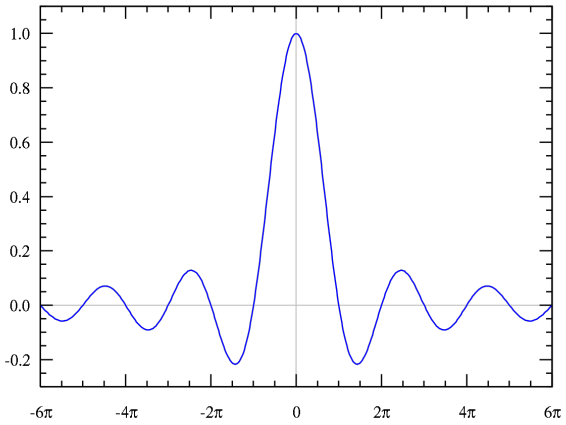

Figure 5.2: Sinc function (unnormalized). [105]

The sinc(x) function, 5.2 figure has the absolute maximum at $x = 0$. In the case of SPDC, this means that as Δk_z approaches zero, the more efficient the process becomes. This results in the phase matching relation:

$$\Delta k_z = k_{pz} - k_{sz} - k_{iz} \approx 0. \tag{5.25}$$

Essentially, this means the phase mismatch should be close to zero in order to obtain an effective nonlinear interaction.

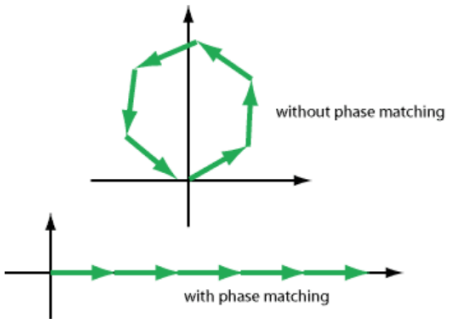

Figure 5.3: Addition of amplitude contributions from different parts of the crystal. Only with phase matching, a high conversion efficiency can be achieved. [106]

In figure 5.3, the arrows illustrate the phasors corresponding to the complex amplitude contributions from different parts of the nonlinear crystal to the harmonic wave. Only when phase matching is achieved,

these contributions add up constructively, and a high power conversion efficiency is achieved.

In the degenerate case, $2\omega_p = \omega_s = \omega_i$ and $k_{pz}/2 = k_{sz} = k_{iz}$, equation 5.25 reduces to:

$$n_p = n_s \cos\theta_c, \tag{5.26}$$

where θ_c is the angle that the signal (or idler) photons form with the direction of propagation of the pump beam inside the crystal. This implies that $n_p \leq n_s$. It is not possible to satisfy this relation in an isotropic medium because for normal dispersion, the index of refraction decreases with increasing wavelength, that is, $n_p > n_s$. This problem can be solved using a birefringent crystal, which has two indices of refraction commonly known as the extra-ordinary (n_e) and ordinary index (n_o) of refraction of the crystal.

In a birefringent crystal, when light enters through an axis different from the optical axis, it is refracted into two rays, each polarized with the vibration directions oriented at right angles (mutually perpendicular) to one another and traveling at different velocities.

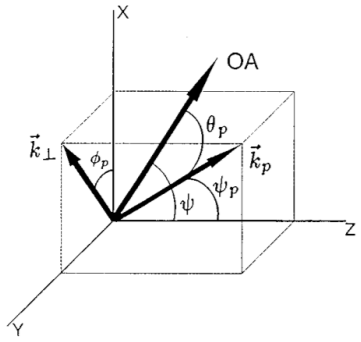

Figure 5.4: A representation of the pump wave vector inside the crystal: the optic axis, OA, lies in the x-z plane making an angle ψ with the z axis. In general, $\vec{k_p}$ does not lie in the x-z plane, but makes an angle θ_p with OA, and an angle ϕ_p with the z axis. $\vec{k_\perp}$ is the projection of $\vec{k_p}$ into the x-y plane, making an angle ϕ_p with the x axis. [107]

In this situation, the wavelengths and wave vectors of the SPDC are determined by the phase-matching angle ψ, the angle formed by the optical axis of the crystal and the wave vector of the pump wave as shown in figure 5.4.

Adjustment of the propagation angle affects the refractive index of the extraordinary beam (called extraordinary refractive index), whereas the ordinary index stays constant. By selecting the correct phase-matching angle, the index of refraction between n_o and n_e can be tuned to satisfy the conditions and, in addition, to control the emission from collinear to non-collinear SPDC.

This technique is relatively sensitive to misalignment of the beams. There is only a finite range of beam angles (the acceptance angle, also called angular phase-matching bandwidth) where critical phase matching works. This also implies that the beam divergence must be limited, and this often forces one to use beams with a large beam radius. Another downside to this method is the spatial walk-off between

ordinary and extraordinary beams, which limits the effective interaction length.

It is important to realize that the choice of phase-matching configuration also influences the effective strength of the nonlinearity, because it determines the directions of the electric fields involved with respect to the crystal axes. For example, there are configurations which would offer a large gain bandwidth but are hardly usable since the effective nonlinearity would be very weak.

In practise, to use this method, it is very useful to have software which can systematically identify all possible phase-matching configurations for a given nonlinear interaction, based on the Sellmeier equations for the refractive indices of all involved waves. A study of these equations and software on how to compute it can be found in [108].

Quasi-phase matching

Previously, to have phase matching conditions, the angle of the pump with the optical axis of the crystal was tuned. This is not the only technique.

Quasi-phase matching is a technique for achieving similar results to those with phase matching of nonlinear interactions. Instead of a homogeneous nonlinear crystal material, a material with spatially modulated nonlinear properties is used.

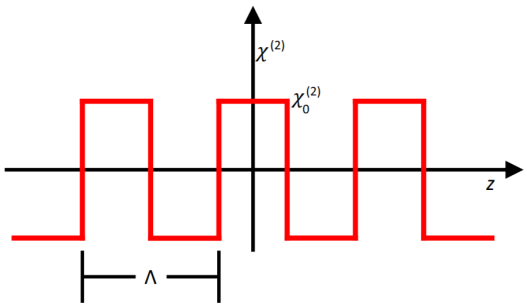

Figure 5.5: Effective nonlinear coefficient in a periodic material. The nonlinear coefficient can be written as a step function, which goes from $-\chi_0^{(2)}$ to $\chi_0^{(2)}$, with a period of Λ. [109]

Using the fact that $\chi^{(2)}(z)$ is an even function, it can be written as a Fourier series:

$$\chi^{(2)}(z) = \sum_{m=-\infty}^{\infty} \frac{2\chi_0^{(2)}}{\pi m} \sin\left(\frac{m\pi}{2}\right) e^{i\frac{2\pi m}{\Lambda}z}. \tag{5.27}$$

Any term of this sum can be used to evaluate the SPDC Hamiltonian. However, it only needed one of these terms to be large in order to get signal. Because the coefficients of the Fourier series get smaller as $|m|$ grows, the term $m = -1$ will be chosen. Then:

$$\chi_{eff}^{(2)} = \frac{2\chi_0^{(2)}}{\pi} e^{-i\frac{2\pi}{\Lambda}z}. \tag{5.28}$$

By substituting this term in equation 5.16, a factor of $2/\pi$ appears but more importantly, the phase matching condition becomes:

$$\Delta k_z = k_{pz} - k_{sz} - k_{iz} - \frac{2\pi}{\Lambda} = 0. \tag{5.29}$$

This is the quasi-phase matching condition. As there is now a new parameter, Λ, it can be tuned to produce the conditions necessary for the SPDC process to occur.

This leads to some clear advantages. First, the period Λ can be chosen such that collinear down-conversion is phasematched.

This makes it much easier to collect all the signal and idler photons produced. The beams can be made to travel along one of the crystal's crystallographic axes. This then eliminates the problems caused by spatial walk-off, and therefore allows the use of much longer crystals, which again leads to an increased signal.

Compared with the perfectly phase-matched case, this method leads to a lower conversion efficiency if the nonlinear coefficient is the same by a factor of $2/\pi$. Nevertheless, the nonlinear coefficient can be chosen with this technique. This means a better coefficient can be chosen and the actual efficiency can be increased overall.

Temperature dependence

Until now, temperature changes to the system have been neglected. This, however, cannot be done because a slight offset to the poling period can result in a completely different functional temperature.

In order to account the temperature, equation 5.29 is written in terms of wavelength:

$$\frac{n_p}{\lambda_p} = \frac{n_s}{\lambda_s} + \frac{n_i}{\lambda_i} + \frac{1}{\Lambda}, \tag{5.30}$$

where n_j represents the temperature dependant index of refraction for the pump, signal and idler. Because of energy conservation, $\lambda_s = (1/\lambda_p - 1/\lambda_s)^{-1}$. Then:

$$\frac{n_p}{\lambda_p} = \frac{n_s}{\lambda_s} + n_i\left(\frac{1}{\lambda_p} - \frac{1}{\lambda_s}\right) + \frac{1}{\Lambda}. \tag{5.31}$$

The change in poling period with temperature change can be written as a parabolic function of the temperature T:

$$\Lambda = \Lambda_0\left[1 + \alpha\left(T - 25°\mathrm{C}\right) + \beta\left(T - 25°\mathrm{C}\right)^2\right]. \tag{5.32}$$

For the temperature dependence of the refractive index, the same approach can be used:

$$\Delta n(\lambda, T) = n_1(\lambda)\left(T - 25°\mathrm{C}\right) + n_2(\lambda)\left(T - 25°\mathrm{C}\right)^2, \tag{5.33}$$

where the coefficient n_1 and n_2 are written as a third order polynomial of inverse wavelengths:

$$n_{1,2}(\lambda) = \sum_{m=0}^{3} \frac{a_m}{\lambda^m}. \tag{5.34}$$

The room temperature values of the corresponding refractive indices can be given by the following Sellmeier equations:

$$\begin{aligned} n_y^2 &= A_y + \frac{B_y}{1 - C_y/\lambda^2} - D_y\lambda^2 \\ n_z^2 &= A_z + \frac{B_z}{1 - C_z/\lambda^2} - \frac{D_z}{1 - E_z/\lambda^2} - F_z\lambda^2 \end{aligned} \tag{5.35}$$

With the temperature dependence of every term in equation 5.31, by substituting all of the coefficients in along with the known poling period of the crystal and wavelength of the pump, the equation can then solve for the wavelength of the signal (and therefore signal) for any given temperature. The coefficients can be found in the appendix of [109].

Using this approach, simulations were used to calculate the wavelengths of SPDC emitted light as a function of temperature for slightly different poling periods.

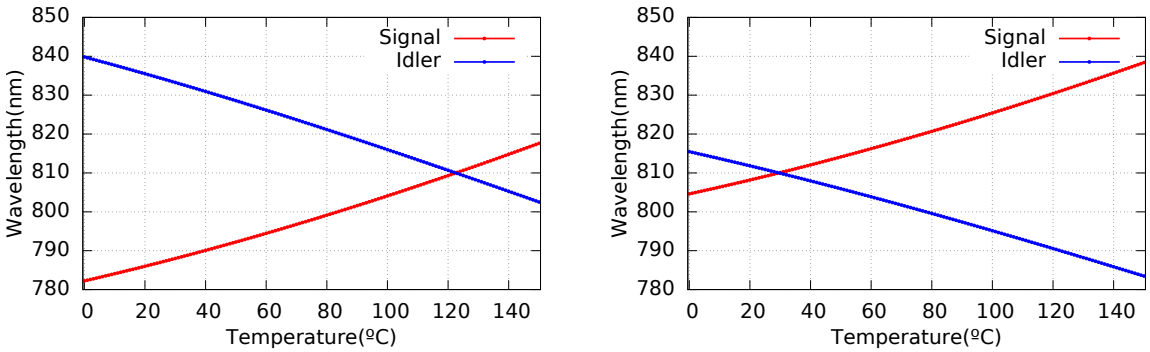

Figure 5.6: Theoretical phase matching curves for PPKTP samples. On the left, a period of $\Lambda = 10\,\mu m$. On the right $\Lambda = 10.35\,\mu m$.

Typical PPKTP samples have a poling period of around $10\,\mu m$. As it can be seen in figure 5.6, the temperature for degenerate SPDC with an exact period of $10\,\mu m$ would be near 120°C. In order to have a degenerate behaviour near room temperatures, the poling period has to be increased. When this value is $10.35\,\mu m$, the temperature is 29.58°C.

Spectral and spatial distribution of the emission

From equation 5.24, the following amplitude can be defined:

$$\Pi(\lambda_s, \lambda_p - \lambda_s, \mathbf{q}_s, \mathbf{q}_i) = \sigma L_z \phi(\lambda_s, \lambda_p - \lambda_s) \text{sinc}\left(\frac{\Delta k_z L_z}{2}\right) G(\mathbf{q}_s + \mathbf{q}_i), \tag{5.36}$$

where $\Pi(\lambda_s, \lambda_p - \lambda_s, \mathbf{q}_s, \mathbf{q}_i)$ is the temperature dependent spectral and spatial amplitude function.

$$\phi(\lambda_s, \lambda_p - \lambda_s) = 2\pi\hbar c \sqrt{\frac{\left(\frac{1}{\lambda_p} - \frac{1}{\lambda_s}\right)\frac{1}{\lambda_s}}{n_s(\lambda_s, T) n_i\left(\left(\frac{1}{\lambda_p} - \frac{1}{\lambda_s}\right)^{-1}, T\right)}}, \tag{5.37}$$

$$\begin{aligned}\Delta k_z =& \sqrt{\left(2\pi\left(\frac{1}{\lambda_p}-\frac{1}{\lambda_s}\right)\right)^2-\mathbf{q}_i^2} \\ &+\sqrt{\left(\frac{2\pi}{\lambda_s}\right)^2-\mathbf{q}_s^2} \\ &-\sqrt{\left(\frac{2\pi}{\lambda_p}\right)^2-(\mathbf{q}_i+\mathbf{q}_s)^2},\end{aligned} \tag{5.38}$$

The assumption of a monochromatic pump beam without normalization function yield a z-independent spectral density:

$$S\left(\lambda_s,\mathbf{q}_s\right)=\int \mathrm{d}^2 q_i \left|\Pi(\lambda_s,\lambda_p-\lambda_s,\mathbf{q}_s,\mathbf{q}_i)\right|^2 \tag{5.39}$$

The symmetry in $\Pi(\lambda_s,\lambda_p-\lambda_s,\mathbf{q}_s,\mathbf{q}_i)$ with respect to $\lambda_p-\lambda_s \leftrightarrow \lambda_s$ and $\mathbf{q}_i \leftrightarrow \mathbf{q}_s$ causes the indistinguishability of signal and idler spectra. Therefore, the total spectrum measured by a spectrometer can be considered to be proportional to the signal spectrum.

The spatial distribution of the beams has been left as a general equation. To see how different assumptions affect the process, different configurations will be studied.

Plane-wave

First, assuming a plane-wave scenario (the simplest approach), the spatial distribution function is independent of $\mathbf{q}_s$ and $\mathbf{q}_i$. Therefore, $G(\mathbf{q}_s+\mathbf{q}_i)\propto C$, where C is a constant.

Then, the spectral density for a given value of $\mathbf{q}_s$ can be plotted as a function of wavelength. These numerically simulated tuning curves are done by calculating equation 5.39 for a given variable set $(\mathbf{q}_s,\lambda_s)$. The integration boundaries for $\mathbf{q_i}$ are limited to an empirically found range where the phase matching condition is fulfilled.

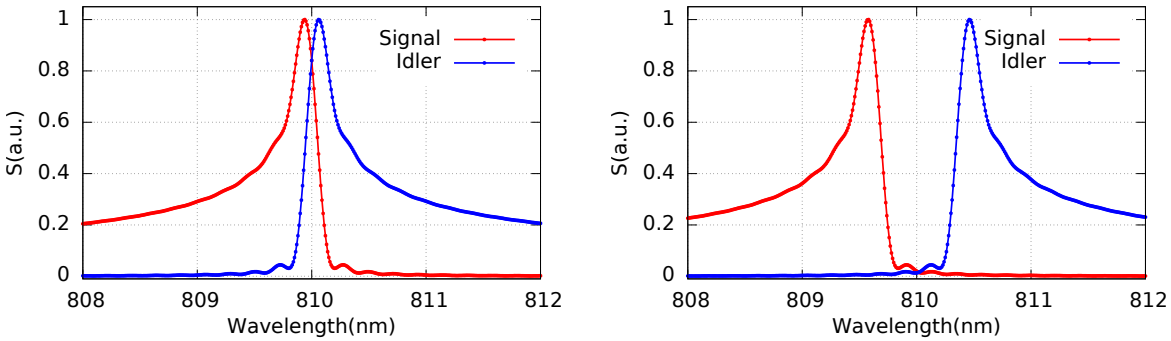

Figure 5.7: Normalized simulated spectral densities for two different values of $|\mathbf{q_s}|$ and a fixed value of temperature. On the left $|\mathbf{q_s}|=0\,\mu m^{-1}$, on the right $|\mathbf{q_s}|=0.5\,\mu m^{-1}$

From figure 5.7, it can be seen that while the behaviour for different values of $|\mathbf{q_s}|$ is the same, as it increases, the maximum value of the spectral emission moves away from the degenerate wavelength. Furthermore, the function decays much faster in one direction than the other. This decay shows similarities with the decay of the Sinc function as it results in an oscillatory evolution away from the center.

From the result for distinct values of $|\mathbf{q_s}|$, it follows that in different directions, the frequency of the emitted photons is different. This gives rise to colored emission rings.

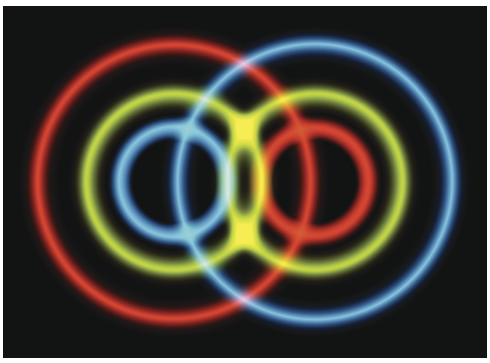

Figure 5.8: Sketch of colored emission rings. [110]

In order to check out its changes with temperature, the same curve was plotted for different values of temperature. As it can be seen in figure 5.9, the behaviour is very similar for different temperatures. The only change is in the emission wavelength, as was already expected from the tuning curves in 5.6.

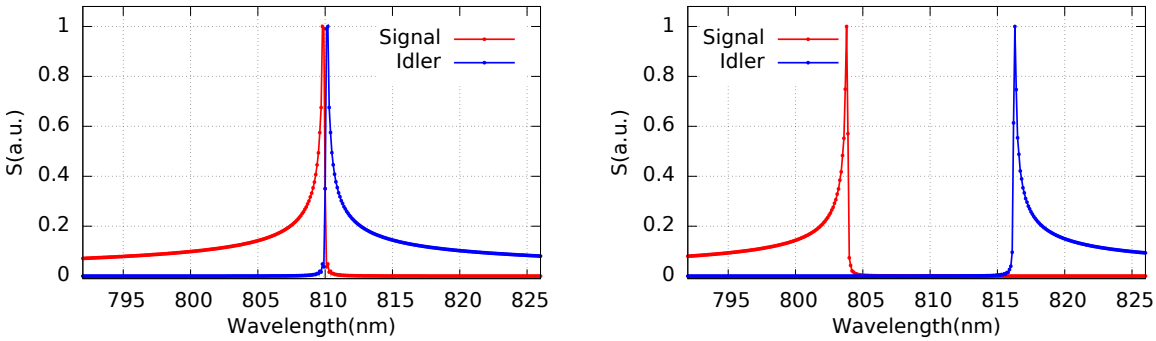

Figure 5.9: Normalized simulated spectral densities for two different temperatures (30°C and 60°C respectively) and a fixed value of transverse momentum ($|\mathbf{q_s}| = 0$).

Gaussian beam

For a Gaussian beam given by:

$$G\left(\mathbf{q}_i + \mathbf{q}_s\right) \propto \exp\left(-\frac{w_0^2\left(\mathbf{q}_i + \mathbf{q}_s\right)^2}{4}\right), \tag{5.40}$$

the following results were obtained.

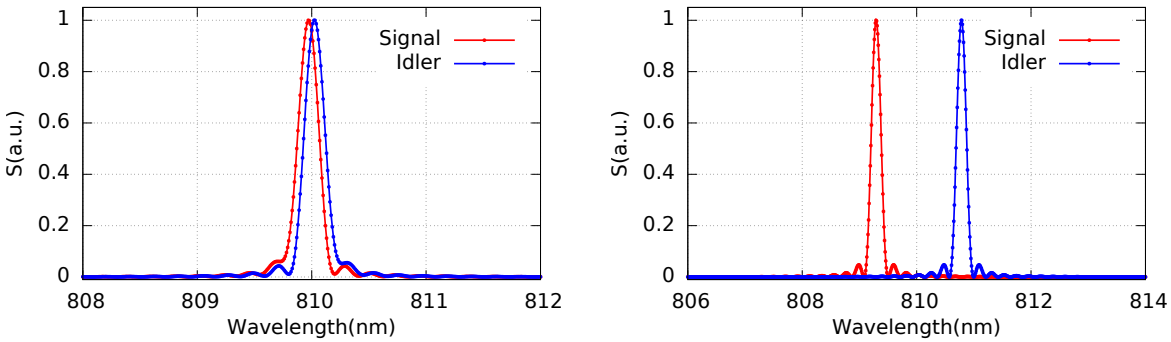

Figure 5.10: Normalized simulated spectral densities for two different values of $|\mathbf{q_s}|$ and a fixed value of temperature. On the left $|\mathbf{q_s}| = 0\,\mu m^{-1}$, on the right $|\mathbf{q_s}| = 0.2\,\mu m^{-1}$

From figure 5.10, a change due to the Gaussian beam assumption can be seen. The emission signal now is almost symmetric around a central wavelength. The slight differences in the oscillations are most likely due to the difference in the refractive index as a function of wavelength. Nevertheless, the typical behaviour of the Sinc function is clearly seen.

Moreover, the central wavelength changes again with $|\mathbf{q_s}|$. This was expected, and the results seen here match those of the literature.

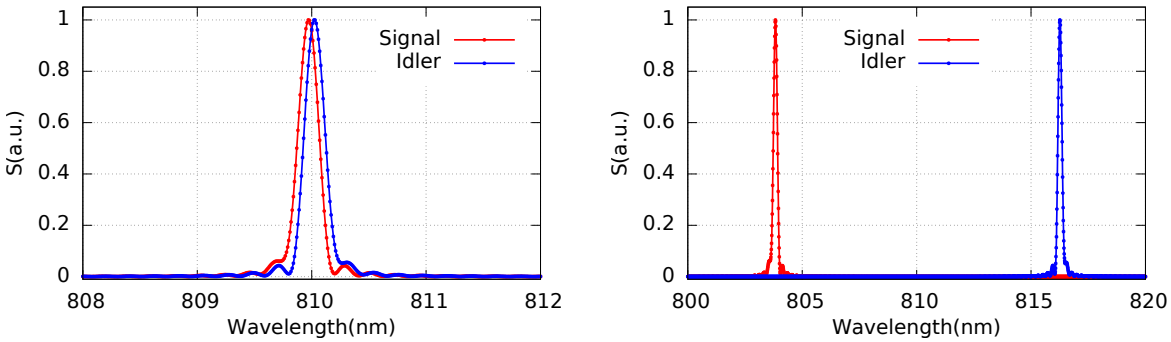

Figure 5.11: Normalized simulated spectral densities for two different temperatures (30°C and 60°C respectively) and a fixed value of transverse momentum ($|\mathbf{q_s}| = 0\,\mu m^{-1}$).

Observing the effect temperature has on the emission spectrum, figure 5.11, we observe the same results. As the temperature changes, the central wavelength shifts. This is important because for the temperature value of 30°C, there is an overlap in the signal's emission and the idler photons. This means they are indistinguishable in wavelength and as a result in frequency. However, when the temperature is changed, this is no longer the case. This fundamental for the generation of entangled pairs.

Besides these plots, coloured plots in which the spectral emission as a function of the wavelength and $|\mathbf{q_s}|$ could be seen were done. Nevertheless, the integrals can result in wrong values due to the behaviour of the functions involved. A careful regime must be given with certain numerical conditions in order for it to converge. As there is still not enough confidence in the results obtained, they are not shown here.

Overall, the plane wave approach is enough if only the central wavelength is desired. For a complete simulation of the typical behaviour, the Gaussian beam approach must be chosen. All these plots

were obtained with equations 5.37 and 5.38 and the equations for the refractive index change due to temperature and wavelength in the software Mathematica.

5.2 Applications

As explained before, SPDC allows the generation of twin photons created at the same time. One of the first application was the localisation of a one-photon state using SPDC, heralded single photons. One photon from the resulting pair may be detected to 'herald' the other (so its state is pretty well known prior to detection).

This is very useful for quantum technologies, since it becomes a single photon emitter. Nevertheless, it is not deterministic, since the appearance of the pair can not be predicted. This can be disadvantageous because some applications need or are better suited with well defined timed events. For example, QKD. However, this limitation can be minimized with the use of pulsed laser sources. Then, the pair is known to have been generated in that interval. However, this brings other problems as a higher power is necessary and the probability of generating multiple pairs increases.

These and other properties have established SPDC as a common source of heralded single photons for proof-of-principle experiments, while other sources are preferred for commercial use.

Another useful application of this effect is in creating entangled pairs. Most commonly, and this work focus, twin photons with orthogonal polarization. This can be used to perform interesting experiments like violating Bell's inequalities, but also to implement other QKD protocols like the E91 protocol previously addressed.

Having a source of entangled photon pairs would allow the pursue of other areas of quantum technologies. One example of this is quantum metrology. Some ideas and proposed designs have been discussed for implementation when a reliable and efficient source is available.

5.3 Progress and future work

As of now, the PPKTP crystal is installed in a Peltier Based Oven. This device controls the temperature of the sample. Some experiments have been performed, but no conclusive results were obtained. Therefore, a complete characterization of the setup is being done. This includes every component from the laser source to the band-pass filters used.

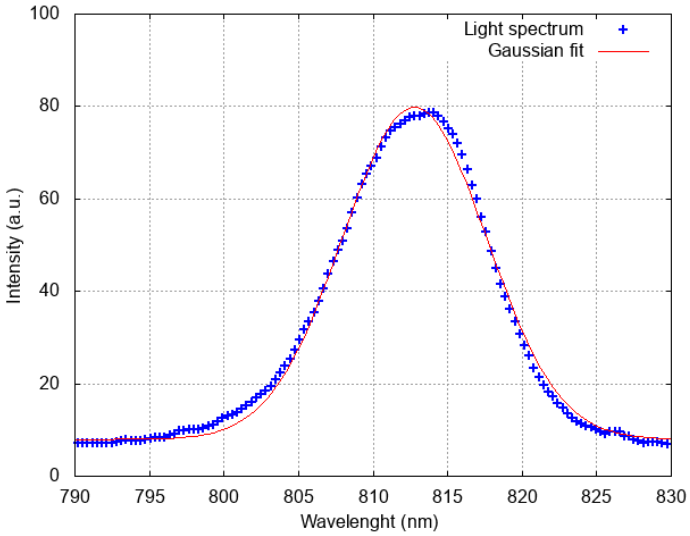

Figure 5.12: Characterization of one of the band-pass filters used.

In figure 5.12, equation 5.41 was adjusted to the light measured by the spectrometer. As it can be seen, the fit matches the measured data well. The central wavelength is shifted to higher values, it was measured as $\lambda_0 = 812.77 \pm 0.03$ nm as opposed to the 810 nm expected. The width of the band-pass filter was measured as $\sigma = 4.83 \pm 0.04$ nm. These results can be seen in the table 5.1 and can be used to further rule out sources of errors in the crystal's characterization. A PASCO spectrometer was used to measure the data and the fitting software Gnuplot to obtain figure 5.12.

$$f(\lambda) = Ae^{-\frac{1}{2}\frac{(\lambda-\lambda_0)^2}{\sigma^2}} + c \tag{5.41}$$

A (a.u)	λ_0(nm)	σ(nm)	c (a.u)	χ^2/ν
71.9±0.4	812.77±0.03	4.83±0.04	8.0±0.2	2.72

For the detection of photons, avalanche photodiodes are being used. These transform the incoming photons into an electric current that can then be observed in conventional devices like an oscilloscope. For the analysis of these currents, the program quTAU is used besides a hardware device to tag the pulses coming from qutools. This allows to measure multiple channels at the same time and it can identify double counts in a defined time window. Therefore, twin photons can be identified and separated from the residual signal that reaches the detector or from dark counts.

In figure 5.13, an image of this software can be seen. The device is connected to a signal generator in order to test it. As it can be seen, it detects the two signals coming in the same window as a coincidence between channel 1 and 2. This means it is performing as expected.

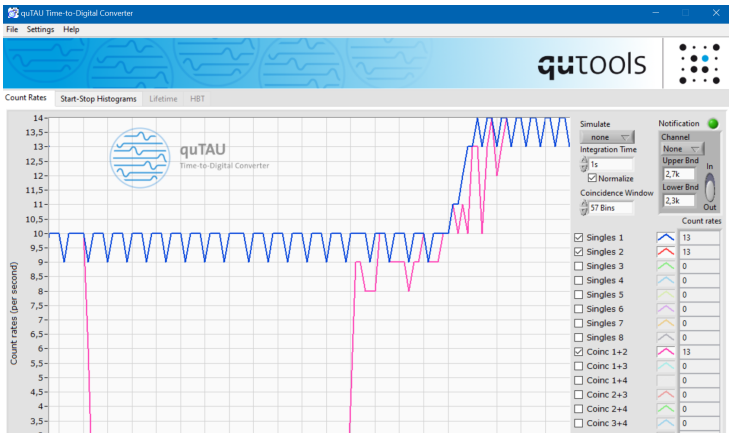

Figure 5.13: Image from the quTau software while it is connected to signal generators to simulate incoming photons.

These were two examples of the characterization being done. The primary goal of this study is to completely characterize the source of photons pairs in order for it to be used in more complicated experiments. The preliminary analysis did not find a significant signal that could be attributed completely to the PPKTP crystal. This could result from many effects. As such, this theoretical study was made to better understand the operation of such an element.

Now, there are some ideas of what can be changed in order to obtain the expected results and then how to improve them in order to achieve maximum efficiency of the source. Nevertheless, those approaches are beyond the scope of this thesis.

Chapter 6

Conclusion and outlook

This work proposes an integrated photonic design for quantum key distribution. The design is small enough for the applications in mind (52×0.5 mm^2). Furthermore, the estimations of the device's losses (4.3 dB) are not prohibitive of its use. However, no prototype was created and characterized. Although similar projects exist in the literature and work, it can not be concluded that this design will perform as expected.

In this project, a different fabrication method was also pursued. By studying and discussion its advantages and disadvantages, it was established as a reliable method with much potential. Nevertheless, its initial cost is high and alternatives to buying a femtosecond laser are being explored.

Moreover, the characterization process of a PPKTP is underway. As the initial tests were inconclusive, a more in depth analysis was necessary. Therefore, a systematic characterization of the elements and a complete theoretical study of the crystal was done. This has pointed to new ideas that will be explored in the future.

All in all, the work developed here was a necessary step forward in bigger projects for the Quantum Technologies group.

Bibliography

[1] J. P. Dowling, G. J. Milburn, *Philosophical Transactions of the Royal Society of London. Series A: Mathematical, Physical and Engineering Sciences* **361**, 1655 (2003).

[2] L. Jaeger, *The Second Quantum Revolution* (Springer, 2018).

[3] D. J. Griffiths, D. F. Schroeter, *Introduction to quantum mechanics* (Cambridge University Press, 2018).

[4] J. J. Sakurai, E. D. Commins, Modern quantum mechanics, revised edition (1995).

[5] P. W. Shor, Polynomial-time algorithms for prime factorization and discrete logarithms on a quantum computer (1995).

[6] J. Clarke, F. K. Wilhelm, *Nature* **453**, 1031 (2008).

[7] A. Steane, *Applied Physics B: Lasers and Optics* **64**, 623–643 (1997).

[8] A. Nizovtsev, *et al.*, *Optics and Spectroscopy* **99**, 233 (2005).

[9] A. Nizovtsev, *et al.*, *Optics and Spectroscopy* **99**, 233 (2005).

[10] V. Giovannetti, S. Lloyd, L. Maccone, *Physical review letters* **96**, 010401 (2006).

[11] G. Cox, *Optical imaging techniques in cell biology* (CRC Press, 2012).

[12] N. Mauranyapin, L. Madsen, M. Taylor, M. Waleed, W. Bowen, *Nature Photonics* **11**, 477 (2017).

[13] J. Abadie, *et al.*, *Nature Physics* **7**, 962 (2011).

[14] A. D. Ludlow, M. M. Boyd, J. Ye, E. Peik, P. O. Schmidt, *Reviews of Modern Physics* **87**, 637 (2015).

[15] C. H. Bennett, G. Brassard, *Theoretical Computer Science* **560**, 7–11 (2014).

[16] Anonymous, Quantum technologies flagship (2020).

[17] E. Diamanti, H.-K. Lo, B. Qi, Z. Yuan, *npj Quantum Information* **2**, 1 (2016).

[18] E. Gibney, *Nature* **535**, 478—479 (2016).

[19] J. Yin, *et al.*, *Science* **356**, 1140 (2017).

[20] J.-G. Ren, *et al.*, *Nature* **549**, 70 (2017).

[21] S.-K. Liao, *et al.*, *Nature* **549**, 43 (2017).

[22] H. Takenaka, *et al.*, *Nature photonics* **11**, 502 (2017).

[23] T. Jennewein, *et al.*, *Advances in photonics of quantum computing, memory, and communication VII* (International Society for Optics and Photonics, 2014), vol. 8997, p. 89970A.

[24] E. Kerstel, *et al.*, *EPJ Quantum Technology* **5**, 6 (2018).

[25] L. Calderaro, *et al.*, *Quantum Information and Measurement (QIM) V: Quantum Technologies* (Optical Society of America, 2019), p. S2A.1.

[26] S. P. Neumann, *et al.*, *EPJ Quantum Technology* **5**, 4 (2018).

[27] D. K. L. Oi, *et al.*, *Contemporary Physics* **58**, 25 (2017).

[28] A. Politi, M. J. Cryan, J. G. Rarity, S. Yu, J. L. O'Brien, *Science* **320**, 646–649 (2008).

[29] R. H. Hadfield, *Nature photonics* **3**, 696 (2009).

[30] C. Santori, D. Fattal, J. Vučković, G. S. Solomon, Y. Yamamoto, *nature* **419**, 594 (2002).

[31] A. Faraon, *et al.*, *Optics express* **16**, 12154 (2008).

[32] D. Lowndes, S. Frick, A. Hart, J. Rarity, *2019 Conference on Lasers and Electro-Optics Europe and European Quantum Electronics Conference* (Optical Society of America, 2019).

[33] P. Sibson, *et al.*, *Nature communications* **8**, 1 (2017).

[34] J. Matthews, A. Politi, A. Stefanov, J. O'Brien, *Nature Photonics* **3**, 346 (2009).

[35] A. Politi, J. Matthews, J. O'Brien, *Science* **325**, 1221 (2009). Author of Publication Reviewed: A Polit, JCF Matthews, JL O'Brien.

[36] T. K. Paraïso, *et al.*, *NPJ Quantum Information* **5**, 42 (2019).

[37] G. D. Marshall, *et al.*, *Optics express* **17**, 12546 (2009).

[38] B. J. Smith, D. Kundys, N. Thomas-Peter, P. Smith, I. Walmsley, *Optics Express* **17**, 13516 (2009).

[39] G. Mélen, Integrated quantum key distribution sender unit for hand-held platforms, Ph.D. thesis, lmu ((2016)).

[40] C. H. Bennett, G. Brassard, *Theor. Comput. Sci.* **560** (2014).

[41] F. Sebastiano, *et al.* (2017), pp. 1–6.

[42] T. J. Harng (2018).

[43] P. W. Shor, J. Preskill, *Physical review letters* **85**, 441 (2000).

[44] D. Bruß, M. Cinchetti, G. M. D'Ariano, C. Macchiavello, *Physical Review A* **62**, 012302 (2000).

[45] H. Wang, Y. Zhao, X. Yu, B. Chen, J. Zhang, *Optical Fiber Communication Conference (OFC) 2019* (Optical Society of America, (2019)).

[46] B. Da Lio, *et al.*, *Applied Physics Letters* **114** (2019).

[47] M. Peev, *et al.*, *New Journal of Physics* **11** (2009).

[48] T. Vergoossen, S. Loarte, R. Bedington, H. Kuiper, A. Ling, *Acta Astronautica* **173**, 164–171 (2020).

[49] J. S. Orcutt, *et al.*, *Opt. Express* **20**, 12222 (2012).

[50] M. T. Wade, M. A. Popović, *Opt. Express* **21**, 10903 (2013).

[51] V. Temnov, K. Sokolowski-Tinten, P. Zhou, A. El-Khamhawy, D. von der Linde, *Physical Review Letters* **97**, 237403 (2007).

[52] K. Sugioka, Y. Cheng, *Applied physics reviews* **1**, 041303 (2014).

[53] R. Osellame, *et al.*, *Applied physics A* **93**, 17 (2008).

[54] V. A. Amorim (2016).

[55] K. Itoh, W. Watanabe, S. Nolte, C. Schaffer, *MRS Bulletin* **31** (2006).

[56] J. Chan, T. Huser, S. Risbud, D. Krol, *Applied Physics A* **76**, 367 (2003).

[57] U. Haken, O. Humbach, S. Ortner, H. Fabian, *Journal of Non-Crystalline Solids* **265**, 9 (2000).

[58] M. Will, S. Nolte, B. N. Chichkov, A. Tünnermann, *Appl. Opt.* **41**, 4360 (2002).

[59] K. M. Davis, K. Miura, N. Sugimoto, K. Hirao, *Opt. Lett.* **21**, 1729 (1996).

[60] O. Efimov, *et al.*, *Optical Materials* **17**, 379 (2001).

[61] J. W. Chan, T. R. Huser, S. H. Risbud, J. S. Hayden, D. M. Krol, *Applied Physics Letters* **82**, 2371 (2003).

[62] A. M. Streltsov, N. F. Borrelli, *J. Opt. Soc. Am. B* **19**, 2496 (2002).

[63] B. Poumellec, M. Lancry, *1st International Workshop on Multiphoton Processes in Glass and Glassy Materials* pp. 91–105 (2006).

[64] J. W. Chan, T. Huser, S. Risbud, D. M. Krol, *Opt. Lett.* **26**, 1726 (2001).

[65] C. Hnatovsky, *et al.*, *Applied Physics A* **84**, 47 (2006).

[66] Y. Shimotsuma, P. G. Kazansky, J. Qiu, K. Hirao, *Phys. Rev. Lett.* **91**, 247405 (2003).

[67] W. Yang, Femtosecond laser writing in transparent materials, Ph.D. thesis, University of Southampton (2008).

[68] L. A. Fernandes, J. R. Grenier, P. R. Herman, J. S. Aitchison, P. V. S. Marques, *Opt. Express* **20**, 24103 (2012).

[69] R. Heilmann, M. Gräfe, S. Nolte, A. Szameit, *Scientific reports* **4**, 4118 (2014).

[70] I. Dyakonov, *et al.*, *Optics Letters* **42**, 4231 (2017).

[71] C.-Y. Wang, J. Gao, X.-M. Jin, *Optics letters* **44**, 102 (2019).

[72] G. Corrielli, *et al.*, *Nature communications* (2014).

[73] I. Pitsios, F. Samara, G. Corrielli, A. Crespi, R. Osellame, *Scientific Reports* (2017).

[74] E. N. Glezer, E. Mazur, *Applied Physics Letters* **71**, 882 (1997).

[75] D. Ashkenasi, *et al.*, *Applied Physics A* **77**, 223 (2003).

[76] M. Sakakura, M. Terazima, Y. Shimotsuma, K. Miura, K. Hirao, *Opt. Express* **15**, 5674 (2007).

[77] H. Sun, *et al.*, *Applied Physics A* **88**, 285 (2007).

[78] S. Gross, M. J. Withford, *Nanophotonics* **4**, 332 (2015).

[79] M. Ams, G. D. Marshall, D. J. Spence, M. J. Withford, *Opt. Express* **13**, 5676 (2005).

[80] C. B. Schaffer, J. F. García, E. Mazur, *Applied Physics A* **76**, 351 (2003).

[81] J. Chovan, F. Uherek, *Radioengineering* **27**, 357 (2018).

[82] P. Dong, *et al.*, *IEEE Journal of Selected Topics in Quantum Electronics* **20**, 150 (2014).

[83] T. Vo-Dinh, *Biomedical photonics handbook: biomedical diagnostics* (CRC press, 2014).

[84] J. L. O'Brien, A. Furusawa, J. Vučković, *Nature Photonics* **3**, 687–695 (2009).

[85] Z. Chaboyer, T. Meany, L. G. Helt, M. J. Withford, M. J. Steel, *Scientific Reports* **5** (2015).

[86] Saleh-Teich, Fundamentals of photonics,, Chap. 7-8 & Rosencher-Vinter, Chap. 9.

[87] G. Keiser, *Optical Fiber Communications* (American Cancer Society, 2003).

[88] J. Gómez-Correa, *et al.*, *American Journal of Physics* (2017).

[89] Y. Jia, F. Chen, J. Vázquez de Aldana, *Optics Express* **20** (2012).

[90] Newport, Fiber optics: Fiber basics, Tech Note #21 Fiber Optics.

[91] R. Paschotta (SPIE, 2010).

[92] L. Binh, *Guided Wave Photonics: Fundamentals and Applications with MATLAB*, Optics and Photonics (CRC Press, 2016).

[93] L. A. Fernandes, J. R. Grenier, P. R. Herman, J. S. Aitchison, P. V. S. Marques, *Opt. Express* **19**, 11992 (2011).

[94] E. Marcatili, S. Miller, *Bell System Technical Journal* (1969).

[95] R. G. Hunsperger, *Integrated optics*, vol. 4 (Springer, 1995).

[96] S. E. Miller, *Bell System Technical Journal* **43** (1964).

[97] A. W. Snyder, J. Love, *Optical waveguide theory* (Springer Science & Business Media, 2012).

[98] L. Sansoni, *Integrated devices for quantum information with polarization encoded qubits* (Springer, 2014).

[99] A. Syahriar, *2008 IEEE International RF and Microwave Conference* (2008).

[100] I. V. Dyakonov, *et al.*, *Opt. Lett.* (2017).

[101] Z. Wang, K. Sugioka, K. Midorikawa, *Applied Physics A* **89**, 951 (2007).

[102] S. E. Harris, M. K. Oshman, R. L. Byer, *Phys. Rev. Lett.* **18**, 732 (1967).

[103] S. Joshi, Entangled photon pairs: Efficient generation and detection, and bit commitment, Ph.D. thesis (2014).

[104] R. Loudon, *The Quantum Theory of Light* (Oxford University Press, 2000).

[105] W. Commons, File:sinc function (unnormalized).svg — wikimedia commons, the free media repository (2020). [Online; accessed 10-November-2020].

[106] R. Paschotta, article on 'phase matching' in the rp photonics encyclopedia (2020). [Online; accessed accessed on 2020-11-11].

[107] T. Pittman, *et al.*, *Physical review. A* **53**, 2804 (1996).

[108] N. Boeuf, *et al.*, *OPTICAL ENGINEERING-BELLINGHAM-INTERNATIONAL SOCIETY FOR OPTICAL ENGINEERING-* **39**, 1016 (2000).

[109] D. R. Hamel, Realization of novel entangled photon sources using periodically poled materials, Master's thesis, University of Waterloo (2010).

[110] S. Jarman, Photons entangled in terms of radial quantum states (2019).